EUROPEAN LABORATORY FOR PARTICLE PHYSICS

CERN-EP/99-170
29 November 1999

Measurements of R_{b}, $A_{\mathrm{FB}}^{\mathrm{b}}$, and $A_{\mathrm{FB}}^{\mathrm{c}}$ in $\mathrm{e^+e^-}$ Collisions at 130 – 189 GeV

The OPAL Collaboration

Abstract

The cross-section ratio $R_{\mathrm{b}} = \sigma(\mathrm{e^+e^-} \to \mathrm{b\bar{b}})/\sigma(\mathrm{e^+e^-} \to \mathrm{q\bar{q}})$ and the bottom and charm forward-backward asymmetries $A_{\mathrm{FB}}^{\mathrm{b}}$ and $A_{\mathrm{FB}}^{\mathrm{c}}$ are measured using event samples collected by the OPAL detector at centre-of-mass energies between 130 and 189 GeV. Events with bottom quark production are selected with a secondary vertex tag, and a hemisphere charge algorithm is used to extract $A_{\mathrm{FB}}^{\mathrm{b}}$. In addition, the bottom and charm asymmetries are measured using leptons from semileptonic decays of heavy hadrons and pions from $\mathrm{D^{*+}} \to \mathrm{D^0}\pi^+$ decays. The results are in agreement with the Standard Model predictions.

(submitted to Eur. Phys. J. C)

The OPAL Collaboration

G. Abbiendi[2], K. Ackerstaff[8], P.F. Akesson[3], G. Alexander[23], J. Allison[16], K.J. Anderson[9], S. Arcelli[17], S. Asai[24], S.F. Ashby[1], D. Axen[29], G. Azuelos[18,a], I. Bailey[28], A.H. Ball[8], E. Barberio[8], R.J. Barlow[16], J.R. Batley[5], S. Baumann[3], T. Behnke[27], K.W. Bell[20], G. Bella[23], A. Bellerive[9], S. Bentvelsen[8], S. Bethke[14,i], S. Betts[15], O. Biebel[14,i], A. Biguzzi[5], I.J. Bloodworth[1], P. Bock[11], J. Böhme[14,h], O. Boeriu[10], D. Bonacorsi[2], M. Boutemeur[33], S. Braibant[8], P. Bright-Thomas[1], L. Brigliadori[2], R.M. Brown[20], H.J. Burckhart[8], P. Capiluppi[2], R.K. Carnegie[6], A.A. Carter[13], J.R. Carter[5], C.Y. Chang[17], D.G. Charlton[1,b], D. Chrisman[4], C. Ciocca[2], P.E.L. Clarke[15], E. Clay[15], I. Cohen[23], J.E. Conboy[15], O.C. Cooke[8], J. Couchman[15], C. Couyoumtzelis[13], R.L. Coxe[9], M. Cuffiani[2], S. Dado[22], G.M. Dallavalle[2], S. Dallison[16], R. Davis[30], A. de Roeck[8], P. Dervan[15], K. Desch[27], B. Dienes[32,h], M.S. Dixit[7], M. Donkers[6], J. Dubbert[33], E. Duchovni[26], G. Duckeck[33], I.P. Duerdoth[16], P.G. Estabrooks[6], E. Etzion[23], F. Fabbri[2], A. Fanfani[2], M. Fanti[2], A.A. Faust[30], L. Feld[10], P. Ferrari[12], F. Fiedler[27], M. Fierro[2], I. Fleck[10], A. Frey[8], A. Fürtjes[8], D.I. Futyan[16], P. Gagnon[12], J.W. Gary[4], G. Gaycken[27], C. Geich-Gimbel[3], G. Giacomelli[2], P. Giacomelli[2], D.M. Gingrich[30,a], D. Glenzinski[9], J. Goldberg[22], W. Gorn[4], C. Grandi[2], K. Graham[28], E. Gross[26], J. Grunhaus[23], M. Gruwé[27], C. Hajdu[31] G.G. Hanson[12], M. Hansroul[8], M. Hapke[13], K. Harder[27], A. Harel[22], C.K. Hargrove[7], M. Harin-Dirac[4], M. Hauschild[8], C.M. Hawkes[1], R. Hawkings[27], R.J. Hemingway[6], G. Herten[10], R.D. Heuer[27], M.D. Hildreth[8], J.C. Hill[5], P.R. Hobson[25], A. Hocker[9], K. Hoffman[8], R.J. Homer[1], A.K. Honma[8], D. Horváth[31,c], K.R. Hossain[30], R. Howard[29], P. Hüntemeyer[27], P. Igo-Kemenes[11], D.C. Imrie[25], K. Ishii[24], F.R. Jacob[20], A. Jawahery[17], H. Jeremie[18], M. Jimack[1], C.R. Jones[5], P. Jovanovic[1], T.R. Junk[6], N. Kanaya[24], J. Kanzaki[24], G. Karapetian[18], D. Karlen[6], V. Kartvelishvili[16], K. Kawagoe[24], T. Kawamoto[24], P.I. Kayal[30], R.K. Keeler[28], R.G. Kellogg[17], B.W. Kennedy[20], D.H. Kim[19], A. Klier[26], T. Kobayashi[24], M. Kobel[3], T.P. Kokott[3], M. Kolrep[10], S. Komamiya[24], R.V. Kowalewski[28], T. Kress[4], P. Krieger[6], J. von Krogh[11], T. Kuhl[3], M. Kupper[26], P. Kyberd[13], G.D. Lafferty[16], H. Landsman[22], D. Lanske[14], J. Lauber[15], I. Lawson[28], J.G. Layter[4], D. Lellouch[26], J. Letts[12], L. Levinson[26], R. Liebisch[11], J. Lillich[10], B. List[8], C. Littlewood[5], A.W. Lloyd[1], S.L. Lloyd[13], F.K. Loebinger[16], G.D. Long[28], M.J. Losty[7], J. Lu[29], J. Ludwig[10], A. Macchiolo[18], A. Macpherson[30], W. Mader[3], M. Mannelli[8], S. Marcellini[2], T.E. Marchant[16], A.J. Martin[13], J.P. Martin[18], G. Martinez[17], T. Mashimo[24], P. Mättig[26], W.J. McDonald[30], J. McKenna[29], E.A. Mckigney[15], T.J. McMahon[1], R.A. McPherson[28], F. Meijers[8], P. Mendez-Lorenzo[33], F.S. Merritt[9], H. Mes[7], I. Meyer[5], A. Michelini[2], S. Mihara[24], G. Mikenberg[26], D.J. Miller[15], W. Mohr[10], A. Montanari[2], T. Mori[24], K. Nagai[8], I. Nakamura[24], H.A. Neal[12,f], R. Nisius[8], S.W. O'Neale[1], F.G. Oakham[7], F. Odorici[2], H.O. Ogren[12], A. Okpara[11], M.J. Oreglia[9], S. Orito[24], G. Pásztor[31], J.R. Pater[16], G.N. Patrick[20], J. Patt[10], R. Perez-Ochoa[8], S. Petzold[27], P. Pfeifenschneider[14], J.E. Pilcher[9], J. Pinfold[30], D.E. Plane[8], B. Poli[2], J. Polok[8], M. Przybycień[8,d], A. Quadt[8], C. Rembser[8], H. Rick[8], S.A. Robins[22], N. Rodning[30], J.M. Roney[28], S. Rosati[3], K. Roscoe[16], A.M. Rossi[2], Y. Rozen[22], K. Runge[10], O. Runolfsson[8], D.R. Rust[12], K. Sachs[10], T. Saeki[24], O. Sahr[33], W.M. Sang[25], E.K.G. Sarkisyan[23], C. Sbarra[28], A.D. Schaile[33], O. Schaile[33], P. Scharff-Hansen[8], J. Schieck[11], S. Schmitt[11], A. Schöning[8], M. Schröder[8], M. Schumacher[3], C. Schwick[8], W.G. Scott[20], R. Seuster[14,h], T.G. Shears[8], B.C. Shen[4], C.H. Shepherd-Themistocleous[5], P. Sherwood[15], G.P. Siroli[2], A. Skuja[17], A.M. Smith[8], G.A. Snow[17], R. Sobie[28], S. Söldner-Rembold[10,e], S. Spagnolo[20], M. Sproston[20], A. Stahl[3], K. Stephens[16], K. Stoll[10], D. Strom[19], R. Ströhmer[33],

B. Surrow[8], S.D. Talbot[1], P. Taras[18], S. Tarem[22], R. Teuscher[9], M. Thiergen[10], J. Thomas[15], M.A. Thomson[8], E. Torrence[8], S. Towers[6], T. Trefzger[33], I. Trigger[18], Z. Trócsányi[32,g], E. Tsur[23], M.F. Turner-Watson[1], I. Ueda[24], R. Van Kooten[12], P. Vannerem[10], M. Verzocchi[8], H. Voss[3], F. Wäckerle[10], D. Waller[6], C.P. Ward[5], D.R. Ward[5], P.M. Watkins[1], A.T. Watson[1], N.K. Watson[1], P.S. Wells[8], T. Wengler[8], N. Wermes[3], D. Wetterling[11] J.S. White[6], G.W. Wilson[16], J.A. Wilson[1], T.R. Wyatt[16], S. Yamashita[24], V. Zacek[18], D. Zer-Zion[8]

[1]School of Physics and Astronomy, University of Birmingham, Birmingham B15 2TT, UK
[2]Dipartimento di Fisica dell' Università di Bologna and INFN, I-40126 Bologna, Italy
[3]Physikalisches Institut, Universität Bonn, D-53115 Bonn, Germany
[4]Department of Physics, University of California, Riverside CA 92521, USA
[5]Cavendish Laboratory, Cambridge CB3 0HE, UK
[6]Ottawa-Carleton Institute for Physics, Department of Physics, Carleton University, Ottawa, Ontario K1S 5B6, Canada
[7]Centre for Research in Particle Physics, Carleton University, Ottawa, Ontario K1S 5B6, Canada
[8]CERN, European Organisation for Particle Physics, CH-1211 Geneva 23, Switzerland
[9]Enrico Fermi Institute and Department of Physics, University of Chicago, Chicago IL 60637, USA
[10]Fakultät für Physik, Albert Ludwigs Universität, D-79104 Freiburg, Germany
[11]Physikalisches Institut, Universität Heidelberg, D-69120 Heidelberg, Germany
[12]Indiana University, Department of Physics, Swain Hall West 117, Bloomington IN 47405, USA
[13]Queen Mary and Westfield College, University of London, London E1 4NS, UK
[14]Technische Hochschule Aachen, III Physikalisches Institut, Sommerfeldstrasse 26-28, D-52056 Aachen, Germany
[15]University College London, London WC1E 6BT, UK
[16]Department of Physics, Schuster Laboratory, The University, Manchester M13 9PL, UK
[17]Department of Physics, University of Maryland, College Park, MD 20742, USA
[18]Laboratoire de Physique Nucléaire, Université de Montréal, Montréal, Quebec H3C 3J7, Canada
[19]University of Oregon, Department of Physics, Eugene OR 97403, USA
[20]CLRC Rutherford Appleton Laboratory, Chilton, Didcot, Oxfordshire OX11 0QX, UK
[22]Department of Physics, Technion-Israel Institute of Technology, Haifa 32000, Israel
[23]Department of Physics and Astronomy, Tel Aviv University, Tel Aviv 69978, Israel
[24]International Centre for Elementary Particle Physics and Department of Physics, University of Tokyo, Tokyo 113-0033, and Kobe University, Kobe 657-8501, Japan
[25]Institute of Physical and Environmental Sciences, Brunel University, Uxbridge, Middlesex UB8 3PH, UK
[26]Particle Physics Department, Weizmann Institute of Science, Rehovot 76100, Israel
[27]Universität Hamburg/DESY, II Institut für Experimental Physik, Notkestrasse 85, D-22607 Hamburg, Germany
[28]University of Victoria, Department of Physics, P O Box 3055, Victoria BC V8W 3P6, Canada
[29]University of British Columbia, Department of Physics, Vancouver BC V6T 1Z1, Canada
[30]University of Alberta, Department of Physics, Edmonton AB T6G 2J1, Canada
[31]Research Institute for Particle and Nuclear Physics, H-1525 Budapest, P O Box 49, Hungary

[32]Institute of Nuclear Research, H-4001 Debrecen, P O Box 51, Hungary
[33]Ludwigs-Maximilians-Universität München, Sektion Physik, Am Coulombwall 1, D-85748 Garching, Germany

[a] and at TRIUMF, Vancouver, Canada V6T 2A3
[b] and Royal Society University Research Fellow
[c] and Institute of Nuclear Research, Debrecen, Hungary
[d] and University of Mining and Metallurgy, Cracow
[e] and Heisenberg Fellow
[f] now at Yale University, Dept of Physics, New Haven, USA
[g] and Department of Experimental Physics, Lajos Kossuth University, Debrecen, Hungary
[h] and MPI München
[i] now at MPI für Physik, 80805 München.

1 Introduction

Many measurements of heavy quark production have been performed in e^+e^- collisions on the Z^0 resonance [1]. Among the measured parameters are the production cross-sections of bottom and charm quark pairs relative to the hadronic cross-section, R_b and R_c, and the forward-backward asymmetries A_{FB}^b and A_{FB}^c. In this paper, measurements of R_b, A_{FB}^b, and A_{FB}^c at energies above the Z^0 resonance are presented for $e^+e^- \to Z^0/\gamma^* \to q\bar{q}$ events, where the effective centre-of-mass energy $\sqrt{s'}$ after initial-state radiation is required to satisfy $\sqrt{s'/s} > 0.85$. Similar measurements have been performed previously by other collaborations [2, 3].

The data collected with the OPAL detector at LEP at centre-of-mass energies between 130 GeV and 189 GeV are analysed. The basic techniques are similar to those adopted in previous OPAL measurements [4–6]. The R_b measurement is based on the selection of a sample enriched in $b\bar{b}$ events obtained with a secondary vertex tagging technique. Both $r\phi$ and rz information[1] from the silicon microvertex detector are used in the selection of $b\bar{b}$ events, improving on [4, 5] where only $r\phi$ information was used. This provides higher efficiency at comparable purity, thus enhancing the statistical precision of the measurement.

Two measurements of forward-backward asymmetries are performed. In the events selected by secondary vertex tagging, the asymmetry A_{FB}^b is measured using a hemisphere charge technique to identify the direction of emission of the primary quark. An independent measurement of both the bottom and charm forward-backward asymmetries is performed using leptons from semileptonic decays of heavy hadrons and pions from $D^{*+} \to D^0\pi^+$ decays. The asymmetries obtained with the hemisphere charge method and the lepton and slow pion methods are combined.

In Section 2, a brief description of the OPAL detector and the event selection is given. The R_b measurement is discussed in Section 3, followed by a description of the asymmetry measurements in Section 4. Systematic errors on both the R_b and asymmetry measurements are given in Section 5, and in Section 6, all results are summarised.

2 The OPAL Detector and Event Selection

A detailed description of the OPAL detector can be found elsewhere [7]. For this analysis, the most relevant parts of the detector are the silicon microvertex detector, the tracking chambers, the electromagnetic and hadronic calorimeters, and the muon chambers. The microvertex detector is essential for the reconstruction of secondary vertices. The central detector provides precise measurements of the momenta of charged particles by the curvature of their trajectories in a magnetic field of 0.435 T. In addition, it allows an identification of charged particles through a combination of the measurement of the specific energy loss dE/dx and the momentum. The electromagnetic calorimeter consists of approximately 12000 lead glass blocks, which completely cover the azimuthal range up to polar angles of $|\cos\theta| < 0.98$. Nearly the entire detector is surrounded with four layers of muon chambers, after approximately one metre of iron from the magnet return yoke, which is instrumented as a hadron calorimeter.

[1] The OPAL coordinate system is defined as a right-handed Cartesian coordinate system, with the x axis pointing in the plane of the LEP collider towards the centre of the ring, the z axis in the direction of the outgoing electrons, and θ and ϕ defined as the usual spherical polar coordinates.

Starting in 1995, the LEP experiments have collected data at increasing energies well above the Z^0 peak. In this paper, the energy points are classified in five different sets, at centre-of-mass energies which will be generically called $\sqrt{s}$=133, 161, 172, 183, and 189 GeV. Table 1 shows the luminosity-weighted mean centre-of-mass energies at which data were taken, and the corresponding integrated luminosities. Additionally, calibration data taken at the Z^0 peak during 1996, 1997, and 1998 are used to cross-check the analyses.

Dataset	133 GeV	161 GeV	172 GeV	183 GeV	189 GeV
$\langle\sqrt{s}\rangle$ (GeV)	133.3	161.3	172.1	182.7	188.6
Integrated luminosity (pb^{-1})	9.9	9.6	9.9	55.8	177

Table 1: The effective centre-of-mass energies and integrated luminosities of data collected above the Z^0 peak. The uncertainties on these quantities have a negligible effect on the analyses presented in this paper.

Hadronic events, $e^+e^- \to q\overline{q}$, are selected based on the number of reconstructed charged tracks and the energy deposited in the calorimeters. The selection of the subsample of non-radiative hadronic events, defined by the requirement $\sqrt{s'/s} > 0.85$, and the identification and rejection of W^+W^- background are described in detail in [5]. The remaining contamination from radiative hadronic events with true effective centre-of-mass energy below $0.85\sqrt{s}$ is 5−10%, depending on the centre-of-mass energy. The residual contamination from four-fermion events (mainly W and Z pairs) is largest at $\sqrt{s} = 189$ GeV, where it is about 8%. These backgrounds to non-radiative hadronic $q\bar{q}$ events are accounted for in the measurements.

Jets are reconstructed using the JADE algorithm [8] with the E0 recombination scheme [9], keeping the invariant mass cut-off $x_{\min} = 49$ GeV^2 fixed at all centre-of-mass energies.

Hadronic events are simulated using the PYTHIA Monte Carlo generator [10]. Heavy quark fragmentation is modelled according to the scheme by Peterson et al. [11] with fragmentation parameters tuned according to the results in [12]. Four-fermion background events are simulated with the grc4f generator [13]. The events are passed through a detailed simulation of the OPAL detector [14] before being analysed using the same procedure as for the data.

3 Measurement of R_{b}

The tagging of $b\bar{b}$ events is based on the long lifetime (∼1.5 ps) and hard fragmentation of b-flavoured hadrons, which give rise to secondary vertices significantly displaced from the primary vertex. The secondary vertex tag described in Section 3.1 allows a clean and efficient reconstruction of $b\bar{b}$ events. In Section 3.2, the measurement of R_{b} with vertex tagged events is described.

3.1 Secondary Vertex Tag

The algorithm used for secondary vertex reconstruction is described in [15]. For the results presented here, a three-dimensional vertex tagging algorithm is used, which takes advantage of the precise z information provided by the OPAL microvertex detector.

The primary vertex in each event is reconstructed as described in [16], incorporating the average beam spot position determined from the measured tracks and the LEP beam-orbit measurements as a constraint. Although the beam spot is less precisely determined at energies above the Z^0 resonance than at the Z^0 peak, the resulting error on the primary vertex position is still small compared to the error on the reconstructed secondary vertex position. The angular acceptance is restricted to $|\cos\theta_T| < 0.9$, where θ_T denotes the polar angle of the thrust axis of the event. Charged tracks used to reconstruct secondary vertices are selected as described in [4] and least three of them are required to form a vertex.

Each hadronic event is divided into two hemispheres by the plane perpendicular to the thrust axis and containing the nominal interaction point. For each reconstructed secondary vertex the signed decay length L is defined as the distance between the secondary and the primary vertex. L is taken to be positive if the secondary vertex is in the hemisphere pointed at by the momentum vector of the jet which contains the vertex, and negative otherwise. The decay length significance L/σ_L is defined as the ratio of the decay length and its error. Secondary vertices with $L/\sigma_L > 8$ are used to tag $b\bar{b}$ events. This cut represents the best compromise between tagging efficiency and purity.

3.2 Determination of R_b from Vertex-Tagged Events

For the measurement of R_b, the number of events tagged by a secondary vertex is determined and corrected for tagging efficiency and background. Due to the limited statistics compared with the data collected at the Z^0 peak, a double tag technique as e.g. in [17] cannot be applied. In order to reduce the sensitivity of the analysis to the detector resolution, a folded tag technique [16] is used: a hemisphere is assigned a tag if it contains a secondary vertex with a decay length significance $L/\sigma_L > 8$, or an anti-tag[2] if it contains a vertex with a decay length significance $L/\sigma_L < -8$. The number of anti-tagged hemispheres is then subtracted from the number of tagged hemispheres. After subtraction of the four-fermion background, the difference between the number of tagged and anti-tagged hemispheres, $N - \overline{N}$, in a sample of $N_{\rm had}$ hadronic events can be expressed as

$$N - \overline{N} = 2N_{\rm had}[(\epsilon_b - \overline{\epsilon}_b)R_b + (\epsilon_c - \overline{\epsilon}_c)R_c + (\epsilon_{uds} - \overline{\epsilon}_{uds})(1 - R_b - R_c)] \ , \qquad (1)$$

where $(\epsilon_b - \overline{\epsilon}_b)$, $(\epsilon_c - \overline{\epsilon}_c)$, and $(\epsilon_{uds} - \overline{\epsilon}_{uds})$ are the differences between the tagging and anti-tagging efficiencies for a given quark flavour. The tagging efficiencies for $u\bar{u}$, $d\bar{d}$, and $s\bar{s}$ events are averaged (uds), since they are very similar. For R_c, the prediction of ZFITTER [18] is used. The four-fermion background is determined from Standard Model production cross-sections and from selection efficiencies estimated from Monte Carlo simulation. The b-purity for the sample with the folded tag is defined as the fraction of $b\bar{b}$ event hemispheres contained in the sample $N - \overline{N}$, and is about 75%. The distribution of the decay length significance L/σ_L is shown in Figure 1 for events at 189 GeV centre-of-mass energy, together with the expectation from the Monte Carlo simulation. The relative difference between data and Monte Carlo is below 1% for the folded-tag rate and (8 ± 4)% for the anti-tag rate, which is more sensitive to modelling of the detector resolution. For $L/\sigma_L < -10$, the number of events predicted by Monte Carlo differs by two standard deviations from the number of events in the data. This

[2] In the literature, tagged and anti-tagged events are sometimes referred to as "forward" and "backward" tagged events. This convention is not used here to avoid confusion with the distinction between forward and backward event hemispheres in the asymmetry analyses.

indicates an incomplete simulation of the detector resolution, which is taken into account in the systematic errors as described in Section 5.1.6 below. The agreement between data and simulation is similar at the other centre-of-mass energies.

The selected event sample contains a $5-10\%$ contamination of radiative hadronic events, with one or more energetic photons emitted in the initial state. In these events the effective centre-of-mass energy is reduced to values below $\sqrt{s'/s} = 0.85$ where the predicted value of $R_{\rm b}$ is up to 30% larger. In addition, the selection of non-radiative events is around 3% less efficient for $\rm b\overline{b}$ final states than for other flavours, because of a larger missing energy due to neutrinos in semileptonic b hadron decays. The results are corrected for these effects, which are estimated from Monte Carlo simulation. The measured values of $R_{\rm b}$ are also corrected for interference between initial and final-state radiation as described in [4]. This correction comes from the fact that Monte Carlo, which is used to model the data, does not contain interference between initial and final-state radiation.

The numbers of selected events and of tagged and anti-tagged hemispheres are given in Table 2. The differences in hemisphere tagging efficiency, also listed in Table 2, have been determined from Monte Carlo simulation. Their errors include all the systematic uncertainties that will be described in Section 5.1. No systematic uncertainties other than those due to Monte Carlo statistics and detector resolution are assigned to the efficiencies in $\rm u\overline{u}$, $\rm d\overline{d}$, and $\rm s\overline{s}$ events, as they represent a small fraction of the tagged sample. The systematic error is dominated by the uncertainties from the event selection, the modelling of b and c fragmentation and decay, and from the simulation of the detector resolution.

Energy	Events	N	$\overline{N}$	Tagging efficiency differences	$R_{\rm b}$	$R_{\rm b}^{\rm SM}$
133 GeV	745	153	11	$\epsilon'_{\rm b} = 0.347 \pm 0.026$ $\epsilon'_{\rm c} = 0.045 \pm 0.009$ $\epsilon'_{\rm uds} = 0.0035 \pm 0.0014$	0.190±0.023±0.007	0.184
161 GeV	347	58	4	$\epsilon'_{\rm b} = 0.331 \pm 0.013$ $\epsilon'_{\rm c} = 0.045 \pm 0.002$ $\epsilon'_{\rm uds} = 0.0090 \pm 0.0010$	0.195±0.035±0.007	0.171
172 GeV	228	23	3	$\epsilon'_{\rm b} = 0.338 \pm 0.012$ $\epsilon'_{\rm c} = 0.041 \pm 0.002$ $\epsilon'_{\rm uds} = 0.0066 \pm 0.0010$	0.091±0.034±0.005	0.168
183 GeV	1186	232	25	$\epsilon'_{\rm b} = 0.351 \pm 0.009$ $\epsilon'_{\rm c} = 0.048 \pm 0.002$ $\epsilon'_{\rm uds} = 0.0084 \pm 0.0008$	0.213±0.020±0.009	0.165
189 GeV	3209	551	87	$\epsilon'_{\rm b} = 0.363 \pm 0.008$ $\epsilon'_{\rm c} = 0.053 \pm 0.002$ $\epsilon'_{\rm uds} = 0.0099 \pm 0.0008$	0.158±0.012±0.007	0.164

Table 2: The numbers of selected non-radiative events, tagged (N) and anti-tagged ($\overline{N}$) hemispheres, and tagging efficiency differences $\epsilon'_{\rm q} = (\epsilon_{\rm q} - \overline{\epsilon}_{\rm q})$ in the $R_{\rm b}$ analysis. The errors on the tagging efficiencies include systematic uncertainties. The $R_{\rm b}$ results with the statistical and systematic errors and their Standard Model expectations are given in columns 6 and 7.

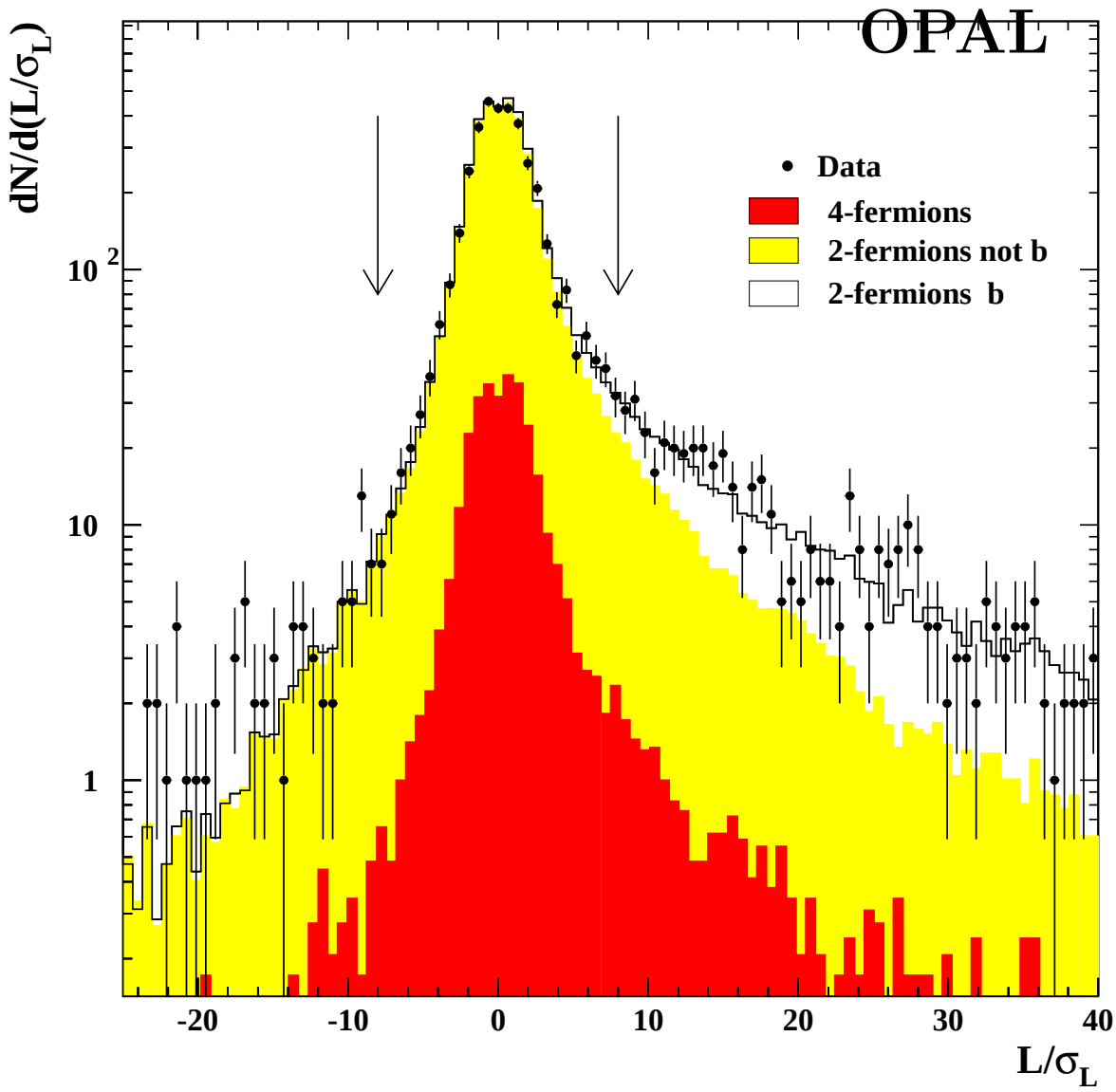

Figure 1: The decay length significance distribution for selected events at 189 GeV centre-of-mass energy. Only the most significant value is used for each event. The points with error bars represent the data. The dark-shaded histogram represents the expected contribution from four-fermion background, and the light-shaded area corresponds to the background from non-$b\bar{b}$ two-fermion events. The unshaded histogram indicates the $b\bar{b}$-content in the sample. The arrows show the position of the cut.

The dependence of the result on the assumed value of R_c can be parametrised as

$$\Delta R_b = b \left(R_c - R_c^{SM} \right) . \quad (2)$$

The parameter b has been determined separately for each centre-of-mass energy. Its values are given in Table 3.

Dataset	133 GeV	161 GeV	172 GeV	183 GeV	189 GeV
$b \equiv (\Delta R_b) / \left(R_c - R_c^{SM} \right)$	−0.12	−0.11	−0.11	−0.12	−0.13
R_c^{SM}	0.223	0.244	0.249	0.253	0.255

Table 3: The dependence of the measured R_b value on the assumed value of R_c for each centre-of-mass energy. The parameter b gives the change in R_b for an assumed deviation of R_c from its Standard Model prediction.

As a cross-check, the analysis is repeated on calibration data collected at the Z^0 peak. A value of $R_b(\sqrt{s} = m_{Z^0}) = 0.221 \pm 0.002(\text{stat.}) \pm 0.010(\text{syst.})$ is obtained. The systematic error has been determined as for the high-energy data samples. This result agrees within the errors with the LEP1 combined value of $R_b^0 = 0.21664 \pm 0.00076$ [1] and can be regarded as a check of the evaluation of systematic errors for the measurements at energies above the Z^0 peak. Note that the 4% systematic error which is assigned to the R_b measurement at $\sqrt{s} = 189$ GeV is larger than the 2% difference with respect to the LEP1 average which is observed at $\sqrt{s} = m_{Z^0}$.

4 Measurement of Forward-Backward Asymmetries

For the measurement of heavy quark forward-backward asymmetries, it is necessary to distinguish the event hemispheres of the primary quark and antiquark in addition to the quark flavour tagging. Two complementary techniques are used. The first analysis provides a measurement of A_{FB}^b for the events that have been tagged by the presence of a secondary vertex. A hemisphere charge method is used to distinguish between quark and anti-quark hemispheres.

The second technique is used for a simultaneous measurement of A_{FB}^b and A_{FB}^c. It is based on the identification of leptons from semileptonic decays of heavy hadrons ("prompt leptons") and pions from $D^{*+} \to D^0\pi^+$ decays ("slow pions"). The charge of these particles provides a clean distinction between the primary quark and anti-quark hemispheres.

In Section 4.1, the measurement of A_{FB}^b with the hemisphere charge technique is described. After a discussion of the lepton and slow pion identification in Section 4.2 and the flavour separation of the tagged samples (Section 4.3), the asymmetry measurement based on prompt leptons and slow pions is presented in Section 4.4. Finally, the combination of the two measurements is treated in Section 4.5.

4.1 Measurement of A_{FB}^b with a Hemisphere Charge Technique

To obtain a sample enriched in $b\bar{b}$ events suitable for the A_{FB}^b measurement, the secondary vertex algorithm used for the R_b analysis is employed. The analysis is limited to the range

$|\cos\theta_T| < 0.9$. Only tagged events are used, since Monte Carlo studies show that with the current statistics, the folded tag would result in a larger error on the forward-backward asymmetry. Thus, an event is considered if it contains a secondary vertex with a decay length significance $L/\sigma_L > 8$ and no other secondary vertex with $L/\sigma_L < -8$. This cut is chosen to minimize the overall error.

Each non-radiative hadronic event is divided into two hemispheres by the plane perpendicular to the thrust axis that contains the nominal interaction point. Monte Carlo simulation shows that the direction of the thrust axis is a good approximation of the direction of emission of the initial $\mathrm{q\overline{q}}$ pair. For each hemisphere, the hemisphere charge Q_{hem} is computed as

$$Q_{\mathrm{hem}} = \frac{\sum_{i=1}^{n} |p_i|^{\kappa} \cdot Q_i}{\sum_{i=1}^{n} |p_i|^{\kappa}}, \tag{3}$$

where the sum runs over all n tracks in the hemisphere, p_i is the momentum component of track i along the thrust axis, Q_i denotes its charge, and $\kappa = 0.4$ is a parameter tuned on simulated events for an optimal charge identification of a primary b or $\overline{\mathrm{b}}$. To ensure a good hemisphere charge reconstruction, only events with more than three charged tracks per hemisphere are used. Events are classified according to the sign of the difference $Q_F - Q_B$ between the forward (Q_F) and backward (Q_B) hemisphere charges, where the forward hemisphere is defined as the one that contains the momentum vector of the incoming electron.

In order to ensure that each event is used at most once in this analysis and the measurement based on prompt leptons and slow pions described below, every event is assigned a figure of merit $\mathcal{P}_{\mathrm{sig}}^{(\mathrm{vtx})}$ defined as

$$\mathcal{P}_{\mathrm{sig}}^{(\mathrm{vtx})} = \tilde{F}_{\mathrm{b}} \cdot (2\tilde{P}_{\mathrm{b}} - 1)\,, \tag{4}$$

where $\tilde{F}_{\mathrm{b}}$ denotes the estimated $\mathrm{b\bar{b}}$ purity as a function of decay length significance and $\tilde{P}_{\mathrm{b}}$ stands for the estimated probability of correct charge identification[3] as a function of $|Q_F - Q_B|$, both determined from the simulation. Events are rejected from the vertex-tagged sample if they are also tagged by the presence of a prompt lepton or slow pion with a corresponding figure of merit $\mathcal{P}_{\mathrm{sig}}^{(\ell/\pi_s)} > \mathcal{P}_{\mathrm{sig}}^{(\mathrm{vtx})}$, where $\mathcal{P}_{\mathrm{sig}}^{(\ell/\pi_s)}$ is determined according to Equation 12 (see Section 4.3 below). At $\sqrt{s} = 189$ GeV, the events that contain both a tagged secondary vertex and a prompt lepton or slow pion correspond to 56% of the vertex tagged and 28% of the lepton or slow pion tagged samples, respectively. Of these common events, 58% are assigned to the secondary vertex tagged event sample by the procedure described above. It has been checked that systematic cross-dependences between the two asymmetry measurements, which may in principle be introduced by this method, are negligibly small. Note that the quantity $\mathcal{P}_{\mathrm{sig}}^{(\mathrm{vtx})}$ is not used in the fit which determines $A_{\mathrm{FB}}^{\mathrm{b}}$, but only to define the selected sample of events.

For the final vertex-tagged event sample, the tagging efficiencies for each flavour are determined from Monte Carlo and are shown in Table 4. The uncertainties include the systematic errors, which will be discussed in detail in Section 5.1. They are dominated by uncertainties in the bottom and charm physics modelling and detector resolution, as in the R_{b} analysis. The b purity is about 60%, with a fraction of four-fermion background up to 5%. The lower b purity with respect to the folded tag purity does not limit the precision of the asymmetry measurement with the present statistics. Because of the rejection of some of the events that are also lepton or slow pion tagged, the final $\mathrm{b\bar{b}}$ efficiencies and purities are lower than those which could otherwise be obtained for a vertex-tagged event sample.

[3]The charge identification probability $\tilde{P}_{\mathrm{b}}$ does not depend significantly on the decay length significance of the tagged vertex.

Flavour q	Event selection efficiency ϵ_q	Charge identification probability P_q
d	0.032 ± 0.005	0.673 ± 0.021
u	0.036 ± 0.005	0.743 ± 0.015
s	0.035 ± 0.005	0.683 ± 0.020
c	0.097 ± 0.005	0.645 ± 0.011
b	0.383 ± 0.025	0.683 ± 0.012

Table 4: Event tagging efficiencies ϵ_q and charge identification probabilities P_q at $\sqrt{s} = 189$ GeV, as determined from Monte Carlo simulation. The efficiencies and charge identification probabilities are computed for the final selected samples after rejection of events with $\mathcal{P}_{\rm sig}^{(\ell/\pi_s)} > \mathcal{P}_{\rm sig}^{(\rm vtx)}$. Similar values have been obtained for the other centre-of-mass energies.

The quantities P_q are the probabilities for the hemisphere charge method to correctly identify the event hemisphere into which the primary quark q was emitted. They are determined from Monte Carlo simulation and are given in Table 4 for the different quark flavours at $\sqrt{s} = 189$ GeV. Similar values are obtained at different centre-of-mass energies. Their errors include systematic uncertainties which will be discussed in detail in Section 5.1. The largest contribution to the systematic error of the b and c quark charge identification probabilities arises from the modelling of heavy flavour fragmentation and decay. For light flavours the uncertainties on fragmentation are expected to have a small effect on the total systematic error, and only Monte Carlo statistics and detector resolution are considered. Possible detector biases in the charge identification probability for positive and negative quarks have been investigated using Z^0 calibration data, and have been found to be negligible.

The quantity

$$x = -\text{sign}(Q_F - Q_B) \cdot |\cos\theta_T| \tag{5}$$

is computed for each event, where θ_T denotes the polar angle of the thrust axis. Its observed distribution at 189 GeV centre-of-mass energy is compared with the Monte Carlo prediction in Figure 2. When only vector and axial vector couplings of the quarks to a gauge boson exchanged in the s-channel are allowed, the observed angular distribution of the primary quark can be expressed as [19]

$$\frac{d\sigma^{obs}}{dx} = \mathcal{C}\,\epsilon(x)\,(1 + x^2 + \frac{8}{3}A_{\rm FB}^{obs}x)\,, \tag{6}$$

where the quark masses have been neglected. The constant $\mathcal{C}$ is for normalization, and $\epsilon(x)$ is the tagging efficiency as a function of $\cos\theta_T$ for an event. It is assumed that the efficiencies are symmetric functions of x, and it has been checked in the simulation that their dependence on x is the same for all primary flavours. For other event types (e.g. four-fermion events), the predicted differential cross-section is not a second-order polynomial, but the resulting effects are negligible within the precision of the measurements presented here.

Using Equation 6, the observed asymmetry $A_{\rm FB}^{obs}$ is obtained by maximising the log likelihood

$$\ln\mathcal{L} = \sum_{j=1}^{N} \ln\{\mathcal{C}\epsilon(x_j)\} + \sum_{j=1}^{N} \ln\left\{1 + x_j^2 + \frac{8}{3}A_{\rm FB}^{obs}x_j\right\}\,, \tag{7}$$

where the sum is over all N selected events, and $A_{\rm FB}^{obs}$ is the only free parameter in the fit. The first term is a constant for a given set of events.

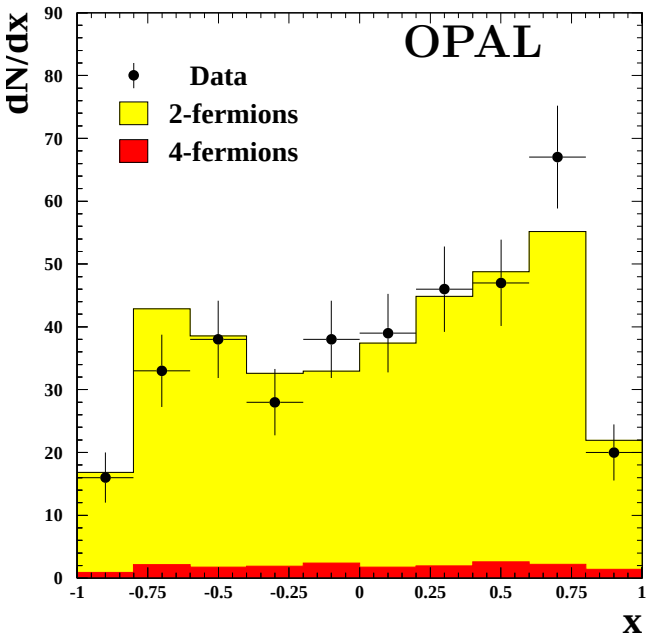

Figure 2: The distribution of the observed $x = -\text{sign}(Q_F - Q_B) \cdot |\cos\theta_T|$ at 189 GeV centre-of-mass energy. The points with error bars are the data, and the histogram is the Monte Carlo expectation. The dark shaded histogram represents the expected contribution from four-fermion background. The histogram showing the Monte Carlo expectation has been scaled to the same number of entries as found in the data.

After four-fermion background subtraction, $A_{\rm FB}^{\rm b}$ is determined from the relation

$$A_{\rm FB}^{obs} = \sum_{\rm q=u,d,s,c,b} s_{\rm q} \cdot F_{\rm q} \cdot (2P_{\rm q} - 1) \cdot A_{\rm FB}^{\rm q} \ . \tag{8}$$

Here, $s_{\rm q}$ is -1 $(+1)$ for up-type (down-type) quarks, and $A_{\rm FB}^{\rm q}$ is the forward-backward asymmetry for flavour q. The asymmetries for non-b events are fixed to their Standard Model values as calculated by ZFITTER. The fractions $F_{\rm q}$ of events of flavour q in the sample are determined as

$$F_{\rm q} = \frac{R_{\rm q}\epsilon_{\rm q}}{\sum_j R_j \epsilon_j} \ , \tag{9}$$

where $R_{\rm q}$ is the ratio of the cross-section of quark type q to the total hadronic cross-section, determined from ZFITTER, and $\epsilon_{\rm q}$ is the tagging efficiency determined from Monte Carlo. The factor $(2P_{\rm q} - 1)$ is to account for charge misassignment. The small contamination from four-fermion events is evaluated as for the $R_{\rm b}$ measurement and subtracted from the sample. Its observed asymmetry is found to be consistent with zero within the available Monte Carlo statistics.

The numbers of tagged events, the observed asymmetries $A_{\rm FB}^{obs}$, and the corrected asymmetries $A_{\rm FB}^{\rm b}$ with their statistical and systematic errors are given in Table 5, together with the Standard Model expectations at the different centre-of-mass energies. Most of the systematic errors are in common with the $R_{\rm b}$ analysis, as discussed below in Section 5.1. The largest systematic errors arise from uncertainties in the detector resolution and the event selection procedure. Uncertainties in the fragmentation of light quarks are assumed to be negligible and are not considered. For all centre-of-mass energies, the statistical error is dominant.

While the observed asymmetries are well within the physical range of $-0.75 < A_{\rm FB}^{obs} < 0.75$, values of $A_{\rm FB}^{\rm b}$ outside this range are possible because of the corrections due to sample composition and charge identification probability. All corrected $A_{\rm FB}^{\rm b}$ values are compatible with a value inside the physical range. No constraint is applied to force the corrected $A_{\rm FB}^{\rm b}$ values to lie within this range, in order to facilitate the combination with the values determined in the lepton and slow pion analysis and with measurements by other experiments.

Energy	Events	$A_{\rm FB}^{obs}$	$A_{\rm FB}^{\rm b}$	$A_{\rm FB}^{\rm b,\,SM}$
133 GeV	75	0.12 ± 0.12	$0.67 \pm 0.50 \pm 0.06$	0.48
161 GeV	35	$-0.17\ ^{+0.18}_{-0.16}$	$-0.59\ ^{+0.76}_{-0.68} \pm 0.04$	0.55
172 GeV	14	$0.32\ ^{+0.27}_{-0.25}$	$1.9 \pm 1.3 \pm 0.1$	0.56
183 GeV	157	$0.182\ ^{+0.082}_{-0.073}$	$1.15\ ^{+0.41}_{-0.37} \pm 0.08$	0.57
189 GeV	372	$0.194\ ^{+0.055}_{-0.047}$	$1.22\ ^{+0.28}_{-0.24} \pm 0.08$	0.58

Table 5: The numbers of tagged events with the vertex tag analysis, the observed asymmetries, the resulting $A_{\rm FB}^{\rm b}$ values, and their Standard Model predictions. The first error on $A_{\rm FB}^{\rm b}$ is statistical, the second systematic.

4.2 Identification of Leptons and Slow Pions

Prompt leptons from semileptonic decays of heavy hadrons provide a means of tagging both $\rm b\bar{b}$ and $\rm c\bar{c}$ events that is largely independent of the secondary vertex tag. In addition, slow pions from $\rm D^{*+} \to D^0\pi^+$ decays are used for tagging heavy flavour events. Both prompt leptons and slow pions allow a clean identification of the event hemisphere that contains the primary quark.

4.2.1 Electron Identification

Electron candidates are required to have a momentum of at least 2 GeV. Tracks with less than 20 $\mathrm{d}E/\mathrm{d}x$ samplings in the tracking chamber are rejected to ensure a good measurement of the specific energy loss. The difference between the measured energy loss and that expected for an electron, divided by the measurement error, is required to be between -2 and 4.

In this sample of preselected tracks, electrons are identified with the help of an artificial neural network, which is described in detail in [17]. In addition to the electron preselection, a network output $\mathcal{N}_{\rm el} > 0.9$ is required. At 189 GeV, this selection has an efficiency for prompt electrons of approximately 25%, defined with respect to the total number of prompt electrons that are reconstructed as tracks in the detector. The resulting sample is 75% pure in electrons.

After this selection, electrons from photon conversions are an important background in the sample. A separate artificial neural network is used to identify pairs of conversion electrons [6,

17]. The contribution from photon conversions is reduced by requiring a network output of $\mathcal{N}_{\rm cv} < 0.4$. In the Monte Carlo simulation at 189 GeV centre-of-mass energy, 89% of the electrons from photon conversions are rejected by this cut, while 90% of the prompt electrons are kept. In Figure 3, the $\mathcal{N}_{\rm el}$ and $\mathcal{N}_{\rm cv}$ output distributions are shown for tracks at 189 GeV centre-of-mass energy.

4.2.2 Muon Identification

The muon selection proceeds in two steps. First, muon track segments are formed from the hits in the muon chambers. Tracks from the central tracking chambers with a momentum greater than 2 GeV are extrapolated to the muon chambers. For each track segment in the muon chambers, only the "best matching track" is considered for use in the asymmetry fit. It is defined as the extrapolated track that has the smallest angular separation α to the muon track segment in question.

In a second step, an artificial neural network trained for muon identification is used to enhance the purity of the muon sample. The network uses the following eleven inputs:

- Information from the matching:
  - The square root of the χ^2 for the position match in θ and ϕ between the extrapolated track and the associated muon track segment in the muon chambers, as described in [20];
  - the ratio of distances $R_{\rm mis} = \alpha^{(1)}/\alpha^{(2)}$ of the best and second best matching track to the muon segment; this is a measure of how ambiguous the choice of the best matching track was in the preselection;
  - the χ^2 probability for the matching computed using both position and direction information for the track in the central detector and the associated muon track segment.
- Information from the hadron calorimeter:
  - The number of calorimeter layers in the cluster associated with the central track;
  - the number of the outermost such layer;
  - the χ^2 probability for the match in θ and ϕ between the track (extrapolated to the hadron calorimeter) and the associated cluster.
- Specific energy loss:
  - The muon $\mathrm{d}E/\mathrm{d}x$ weight for the track, which is a measure of the probability that the track is compatible with a muon hypothesis;
  - $\sigma_{\mathrm{d}E/\mathrm{d}x}$, the error on the $\mathrm{d}E/\mathrm{d}x$ measurement;
  - the momentum of the track.
- Geometrical information:
  - The position in $|\cos\theta|$ and ϕ where the extrapolated track enters the muon chambers.

The distribution of the neural network output $\mathcal{N}_\mu$ is shown in Figure 4 for "best matching" tracks according to the definition above. Muon candidates are retained if $\mathcal{N}_\mu$ is larger than 0.65. In Monte Carlo simulated events at 189 GeV centre-of-mass energy, the muon selection results in an efficiency of 43% for prompt muons, defined with respect to all prompt muons that are reconstructed as tracks, and a muon purity of 73%.

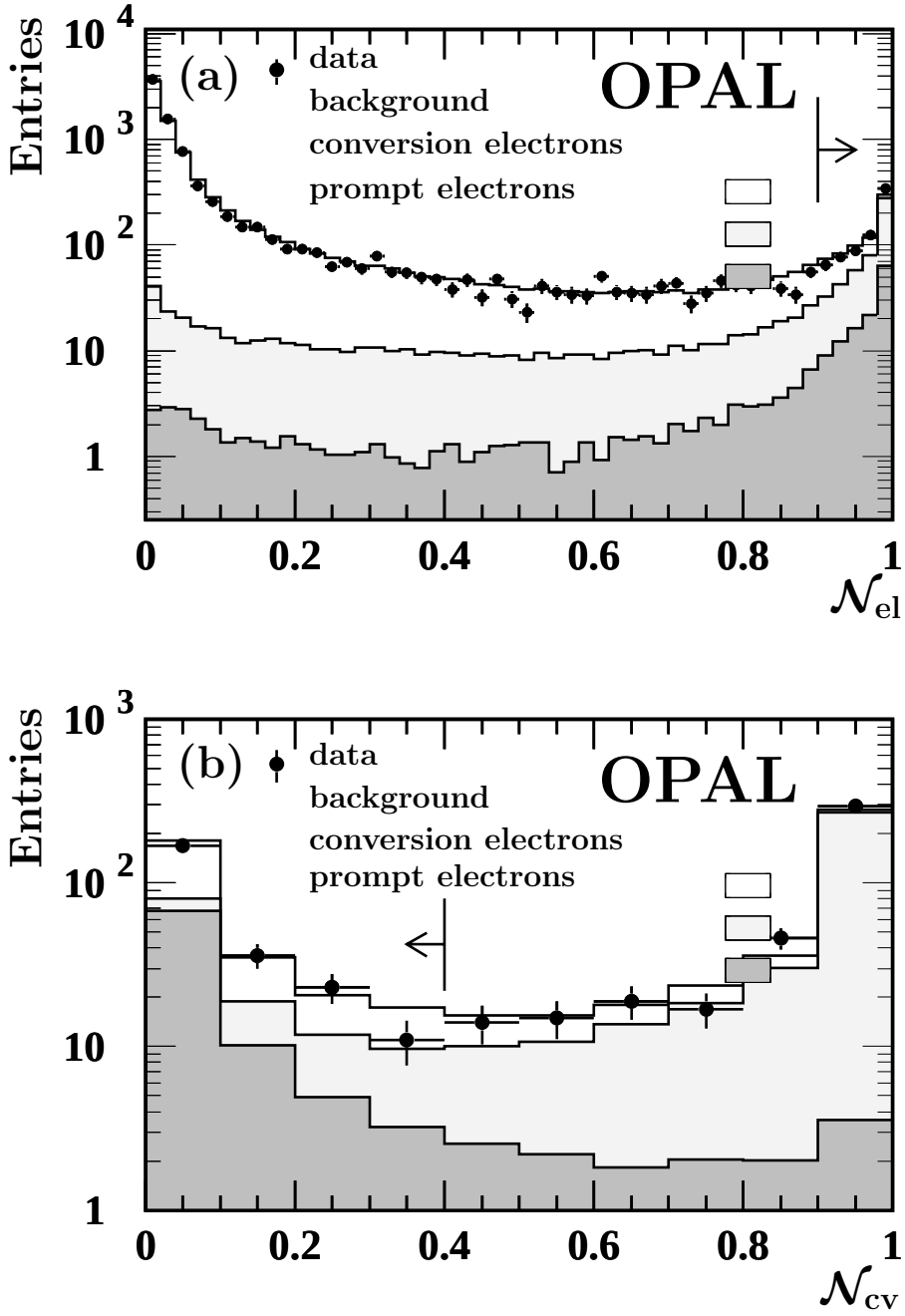

Figure 3: The $\mathcal{N}_{\mathrm{el}}$ distribution is shown in figure (a) for tracks at 189 GeV centre-of-mass energy that pass the electron momentum and $\mathrm{d}E/\mathrm{d}x$ cuts. In (b), the $\mathcal{N}_{\mathrm{cv}}$ distribution is given for those tracks that also pass the requirement of $\mathcal{N}_{\mathrm{el}} > 0.9$. In each case, the points with error bars represent the data distribution, and the histograms the Monte Carlo simulation, scaled to the same number of entries. The dark and light grey areas are the expected contributions from prompt electrons and conversion electrons, respectively, while the open area corresponds to hadrons. The arrows indicate the accepted regions.

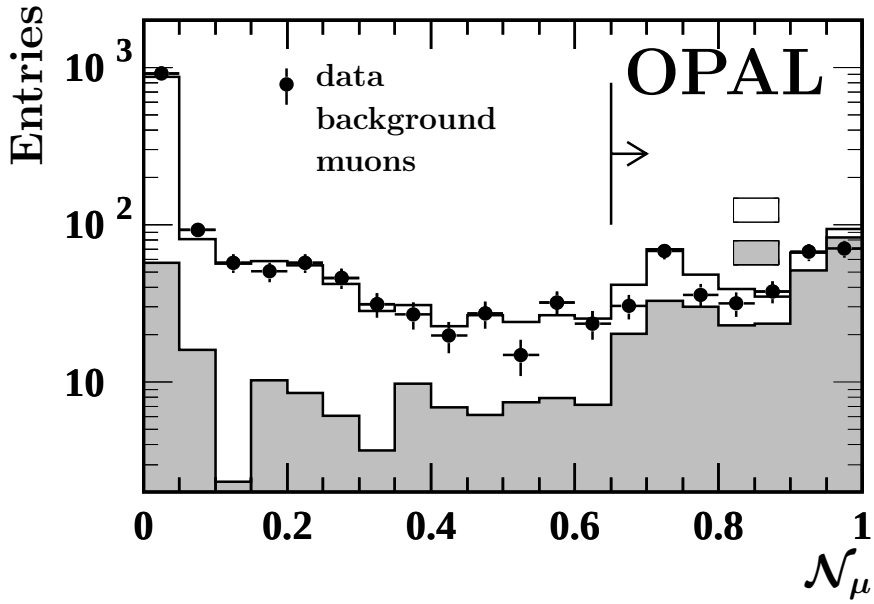

Figure 4: The $\mathcal{N}_\mu$ distribution for best matching tracks at 189 GeV centre-of-mass energy that pass the muon momentum cut. The points with error bars represent the data distribution, and the histogram the Monte Carlo simulation, scaled to the same number of entries. The shaded area is the expected contribution from true muons. The accepted region is indicated by the arrow.

4.2.3 Preselection of Slow Pion Candidates

Pions from $\mathrm{D}^{*+} \to \mathrm{D}^0\pi^+$ decays, denoted π_s in the following, are selected based on the kinematic properties of this decay. Due to the low momentum, $p^* = 39$ MeV [21], of the decay products in the D^{*+} rest frame, pions from this decay have momenta smaller than

$$p_{\pi_s}^{\max} = \frac{\sqrt{s}}{2m_{\mathrm{D}^{*+}}}\,(E^* + p^*) = 0.0458\,\sqrt{s} \tag{10}$$

in the laboratory frame, where $E^* = \sqrt{(p^*)^2 + m_{\pi^+}^2}$, and $m_{\mathrm{D}^{*+}}$ and m_{π^+} denote the D^{*+} and π^+ masses, respectively. In addition, slow pions have a transverse momentum with respect to the D^{*+} flight direction of at most p^*, and are thus dominantly found in the core of the jet containing the D^{*+} meson.

Slow pion candidates are required to have a momentum between 1.0 GeV and $p_{\pi_s}^{\max}$ and, if at least 20 $\mathrm{d}E/\mathrm{d}x$ samplings are available, a specific energy loss $\mathrm{d}E/\mathrm{d}x$ whose probability compatibility for the pion hypothesis exceeds 2%. Tracks that form single charged particle jets are rejected. The D^{*+} flight direction is estimated by the jet direction, which is recalculated in an iterative procedure similar to the one described in [22], based on the rapidities of the tracks and clusters in the jet containing the slow pion candidate. If the jet mass exceeds 2.3 GeV, the track or calorimeter cluster in the jet with the smallest rapidity with respect to the jet axis is removed from the calculation, and the direction is recomputed. The transverse momentum p_t of the slow pion candidate is calculated with respect to this jet direction. The p_t^2 distribution is shown in Figure 5 for tracks at 189 GeV centre-of-mass energy. Slow pion candidates are accepted if $p_t^2 < 0.02$ GeV^2.

In Monte Carlo simulated events at 189 GeV, this preselection is 56% efficient and yields a sample that contains 5.7% of slow pions. This sample is further enriched with a cut that is described in Section 4.3 below.

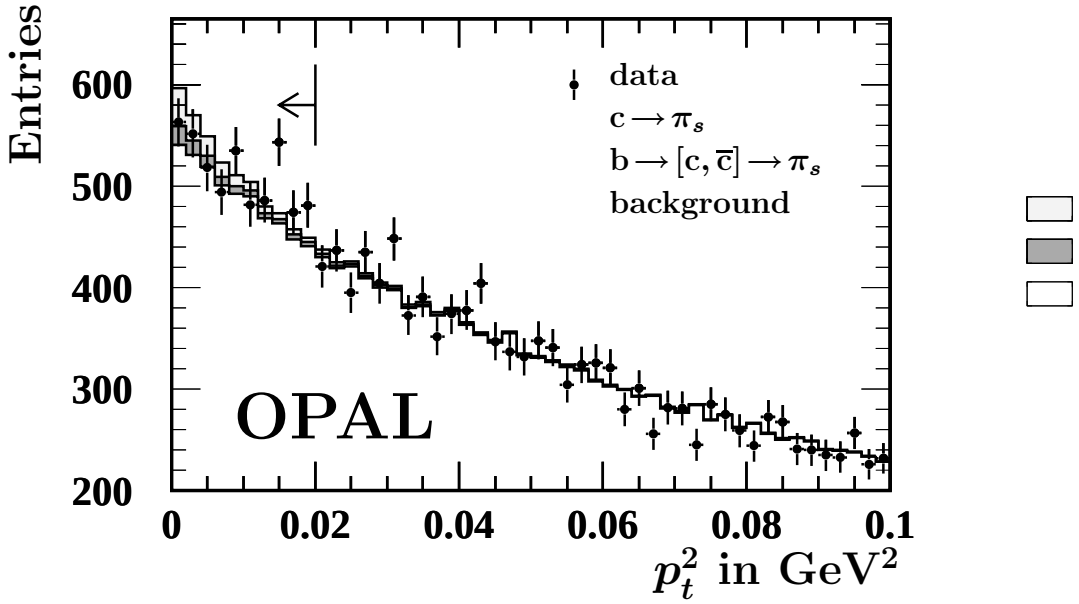

Figure 5: The p_t^2 distribution for tracks at 189 GeV centre-of-mass energy that pass the slow pion momentum and $\mathrm{d}E/\mathrm{d}x$ cuts. Tracks that form single charged particle jets have been excluded. The points with error bars represent the data distribution, and the histogram the Monte Carlo simulation, scaled to the same number of entries. The dark grey area is the expected contribution from true slow pions from cascade $\mathrm{b} \to [\mathrm{c}, \overline{\mathrm{c}}] \to \pi_s$ decays, and the light grey area represents $\mathrm{c} \to \pi_s$ decays. The arrow indicates the accepted region.

4.3 Flavour Separation of the Lepton and Slow Pion Samples

Three different sources of prompt leptons are considered: $\mathrm{b} \to \ell$, meaning leptons from semileptonic decays of b-flavoured hadrons; cascade bottom decays, which include the contributions from $\mathrm{b} \to \mathrm{c} \to \ell$ and $\mathrm{b} \to \overline{\mathrm{c}} \to \ell$ processes; and $\mathrm{c} \to \ell$, leptons from semileptonic decays of charm hadrons. The background can be classified as "non-prompt" leptons, i.e. all other leptons that are not produced in the decay of b- or c-flavoured hadrons, and particles that are mis-identified as electrons or muons.

For electrons and muons, separate artificial neural networks have been constructed with the aim of separating prompt $\mathrm{b} \to \ell$ decays, cascade $\mathrm{b} \to [\mathrm{c}, \overline{\mathrm{c}}] \to \ell$ decays, prompt $\mathrm{c} \to \ell$ decays, and all other contributions. The technique used is similar to the one described in [6], but the inputs and training have been re-optimized for centre-of-mass energies above the Z^0 resonance; also an artificial neural network for the identification of cascade decays is included. Candidates that form single charged particle jets are rejected since they are expected to be dominantly produced in leptonic W decays.

The first network, denoted $\mathcal{N}_{\mathrm{b}}$, is designed to separate $\mathrm{b} \to \ell$ decays from all other contributions. Two networks, $\mathcal{N}_{\mathrm{bc}}$ and $\mathcal{N}_{\mathrm{c}}$, have been trained on a Monte Carlo simulation that does

not contain $b \to \ell$ decays in order to classify lepton candidates that are background to the $\mathcal{N}_b$ net. All three networks use the following input variables, where jet variables are defined with the lepton candidate included in the jet:

- p, the lepton track momentum;
- p_t, the transverse momentum of the lepton track calculated relative to the jet which contains the track;
- L/σ_L, the decay length significances of the secondary vertices (if existing) in the jet containing the lepton and the most energetic jet in the hemisphere not containing the lepton, where secondary vertices are reconstructed with the same algorithm as described in Section 3.1;
- the jet charges of the jets containing the lepton and the most energetic jet in the hemisphere not containing the lepton, each multiplied by the lepton charge, where the jet charge is defined as in Equation 3 with $\kappa = 0.4$, but using only tracks associated to the jet;
- the forward multiplicity in the lepton jet, defined as the number of tracks with an impact parameter significance with respect to the primary vertex larger than 2. For each track, the impact parameter is defined as the distance between the primary vertex and the track at its the point of closest approach; the impact parameter significance is defined as this distance divided by its error;
- the $|\cos\theta|$ of the jet momentum vector, where θ is the jet polar angle;
- the outputs $\mathcal{N}_{\rm el}$ and $\mathcal{N}_{\rm cv}$ of the electron identification network and the conversion finder network, respectively, in the case of electrons;
- the output $\mathcal{N}_\mu$ of the muon identification network, in the case of muons.

From the $\mathcal{N}_b$, $\mathcal{N}_{bc}$, and $\mathcal{N}_c$ network outputs, the following quantities are computed which are related to the probabilities of a lepton candidate to come from one of the three sources:

$$\begin{aligned}
\mathcal{P}_{\rm sig}^{(b\to\ell)} &= \mathcal{N}_b \\
\mathcal{P}_{\rm sig}^{(b\to[c,\overline{c}]\to\ell)} &= (1-\mathcal{N}_b)\,\frac{[\mathcal{N}_{bc}\,(1-\mathcal{N}_c)]}{[\mathcal{N}_{bc}\,(1-\mathcal{N}_c)]+[\mathcal{N}_c\,(1-\mathcal{N}_{bc})]+[(1-\mathcal{N}_c)\,(1-\mathcal{N}_{bc})]} \\
\mathcal{P}_{\rm sig}^{(c\to\ell)} &= (1-\mathcal{N}_b)\,\frac{[\mathcal{N}_c\,(1-\mathcal{N}_{bc})]}{[\mathcal{N}_{bc}\,(1-\mathcal{N}_c)]+[\mathcal{N}_c\,(1-\mathcal{N}_{bc})]+[(1-\mathcal{N}_c)\,(1-\mathcal{N}_{bc})]}\,.
\end{aligned} \tag{11}$$

The difference in the treatment of the $\mathcal{N}_b$ output from $\mathcal{N}_{bc}$ and $\mathcal{N}_c$ is due to the fact that $b \to \ell$ decays were omitted in the training of the latter two networks. Only candidates that satisfy the condition

$$\mathcal{P}_{\rm sig}^{(\ell)} = \sqrt{\left(\mathcal{P}_{\rm sig}^{(b\to\ell)}\right)^2 + \left(\mathcal{P}_{\rm sig}^{(b\to[c,\overline{c}]\to\ell)}\right)^2 + \left(\mathcal{P}_{\rm sig}^{(c\to\ell)}\right)^2} > 0.1 \tag{12}$$

are used in the subsequent analysis. Candidates with lower values of $\mathcal{P}_{\rm sig}^{(\ell)}$ are expected to be dominantly background and to have a negligible contribution to the overall result. Note that the quantity $\mathcal{P}_{\rm sig}^{(\ell)}$, although used to define the selected sample of events, is not itself used in the fit that determines the bottom and charm asymmetries.

Similarly to the lepton case, slow pion candidates are classified as cascade $b \to [c, \overline{c}] \to \pi_s$ decays, $c \to \pi_s$, and background. Another two artificial neural networks, $\mathcal{N}_{bc}$ and $\mathcal{N}_c$, have been trained for the separation of the three components in the preselected slow pion sample. The following inputs are used by both networks:

- p, the slow pion track momentum;

- p_t^2, the transverse momentum squared of the slow pion track calculated relative to the jet direction obtained with the same rapidity based algorithm that is used in Section 4.2.3;
- $E_{\pi_s-\mathrm{jet}}$, the total energy of the jet containing the slow pion;
- $E_{\pi_s-sub-jet}$, the energy of the sub-jet [23] containing the slow pion: Each jet containing a slow pion is split into two sub-jets, where the slow pion sub-jet is seeded by the slow pion track. In an iterative procedure, any particle that forms a smaller opening angle with the slow pion sub-jet than with the remainder of the jet is then assigned to the slow pion sub-jet;
- L/σ_L, the decay length significance of the vertex in the jet containing the slow pion, if a vertex is found;
- the jet charge of the jet containing the slow pion, calculated with $\kappa = 0.4$, multiplied by the slow pion charge; and
- the $|\cos\theta|$ of the jet momentum vector.

In addition, the network for identification of $\mathrm{b} \to [\mathrm{c}, \overline{\mathrm{c}}] \to \pi_s$ decays uses:

- L, the decay length of the vertex (if existing) in the jet containing the slow pion;
- the jet charge of the jet containing the slow pion, calculated with a different parameter $\kappa = 2.0$, multiplied by the slow pion charge;
- the forward multiplicity in the jet containing the slow pion, defined as above;
- $(\sum p_t)_{\mathrm{jet}}$, the scalar sum of the transverse momenta relative to the jet axis of all tracks in the jet; and
- the maximum longitudinal momentum component of any track in the jet containing the slow pion, measured relative to the jet direction.

The quantities $\mathcal{P}_{\mathrm{sig}}^{(\mathrm{b}\to[\mathrm{c},\overline{\mathrm{c}}]\to\pi_s)}$ and $\mathcal{P}_{\mathrm{sig}}^{(\mathrm{c}\to\pi_s)}$ are computed in analogy to Equation 11 for prompt lepton candidates, while $\mathcal{P}_{\mathrm{sig}}^{(\mathrm{b}\to\pi_s)}$ is set to zero. The same requirement on $\mathcal{P}_{\mathrm{sig}}^{(\pi_s)}$ (computed according to Equation 12) is imposed as for prompt leptons.

If more than one lepton or slow pion candidate per event passes the selection, the one with the highest $\mathcal{P}_{\mathrm{sig}}^{(\ell/\pi_s)}$ value is taken. Furthermore, this $\mathcal{P}_{\mathrm{sig}}^{(\ell/\pi_s)}$ value is required to be larger than the value of $\mathcal{P}_{\mathrm{sig}}^{(\mathrm{vtx})}$ as determined for the hemisphere charge measurement (see Section 4.1) if the event is also tagged by the presence of a secondary vertex.

A breakdown of the composition of the samples of electron, muon, and slow pion tagged events at 189 GeV centre-of-mass energy together with the efficiencies is given in Table 6. In Figure 6, the output distributions of the flavour separation networks are shown for the events that pass all cuts.

4.4 Measurement of $A_{\mathrm{FB}}^{\mathrm{b}}$ and $A_{\mathrm{FB}}^{\mathrm{c}}$ with Leptons and Slow Pions

The forward-backward asymmetries for bottom and charm, $A_{\mathrm{FB}}^{\mathrm{b}}$ and $A_{\mathrm{FB}}^{\mathrm{c}}$, are extracted from the data using an unbinned maximum likelihood fit to the charge signed polar angle distribution of the thrust axis $\vec{T}$ in lepton and slow pion tagged events. It is assumed that $\vec{T}$ is the axis along which the primary quark-antiquark pair is emitted. The quantity $y = -q\cos\theta_T$ is computed event by event, where q is the charge of the lepton or slow pion, and the thrust direction $\vec{T}$ is defined such that $\vec{T}\cdot\vec{p} > 0$, with $\vec{p}$ being the momentum of the jet containing the lepton or slow pion. The inclusive y distributions for electron, muon, and slow pion tagged events at 189 GeV are presented in Figure 7.

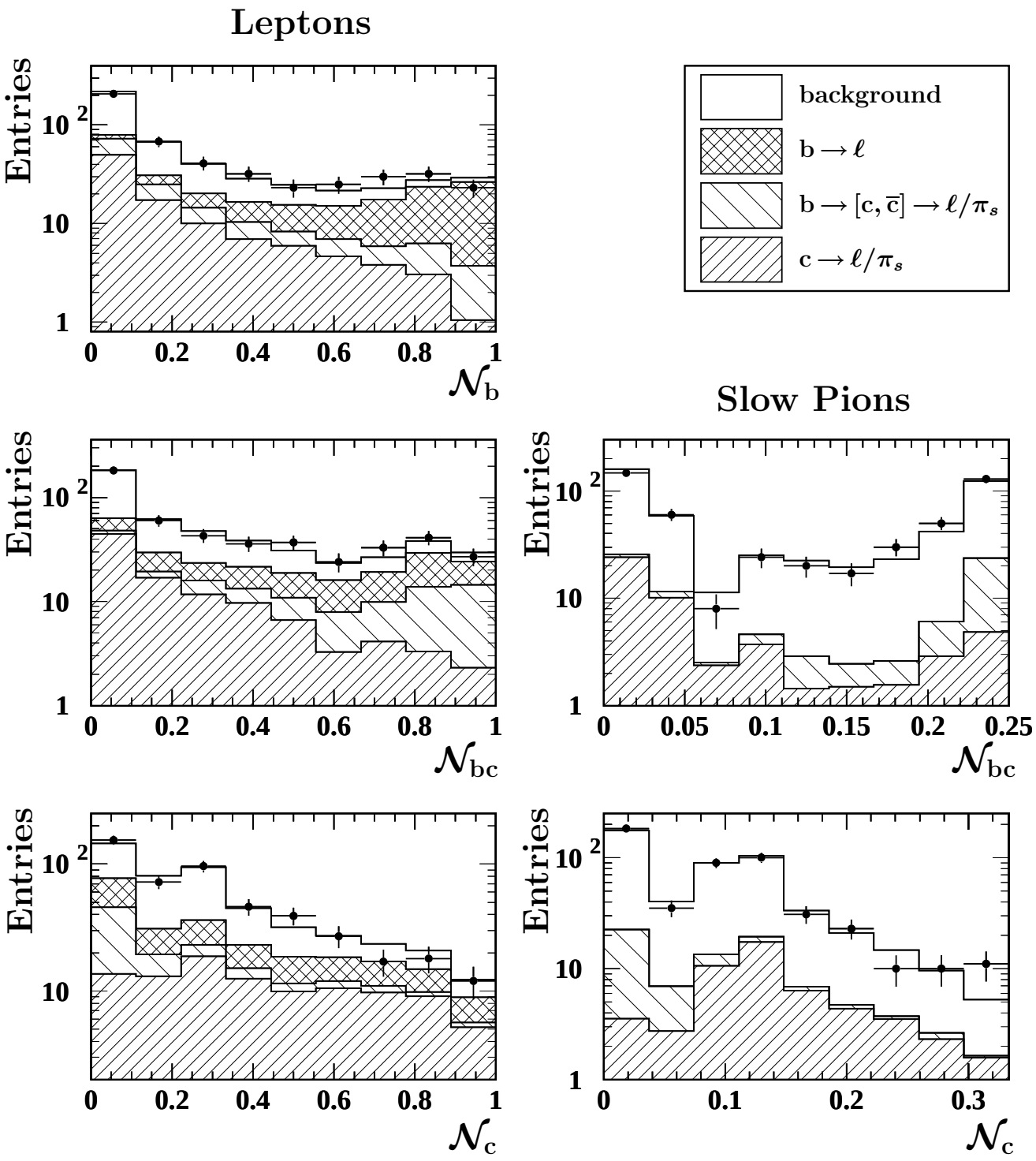

Figure 6: The $\mathcal{N}_{\mathrm{b}}$, $\mathcal{N}_{\mathrm{c}}$, and $\mathcal{N}_{\mathrm{bc}}$ distributions for lepton and slow pion tagged events at 189 GeV centre-of-mass energy. The points with error bars correspond to the data. The open histogram represents the Monte Carlo expectation, where the contributions from signal events are shown hatched as explained in the figure. The purity in the slow pion selection is limited, which is reflected in the fact that the range of $\mathcal{N}_{\mathrm{c}}$ and $\mathcal{N}_{\mathrm{bc}}$ values for slow pions does not extend up to 1.

Source	Sample composition			Efficiencies		
	Electrons	Muons	Slow pions	Electrons	Muons	Slow pions
$b \to \ell$	19 %	19 %	—	26 %	50 %	—
$b \to [c, \overline{c}] \to \ell/\pi_s$	9 %	11 %	3 %	16 %	31 %	6 %
$c \to \ell/\pi_s$	19 %	24 %	13 %	18 %	38 %	13 %
Non-prompt leptons	15 %	20 %	—			
Other background	37 %	25 %	85 %			

Table 6: The estimated composition of the lepton and slow pion tagged event samples at 189 GeV centre-of-mass energy after the selection. The efficiencies of the prompt lepton and slow pion selection are given for the final event sample with respect to all prompt leptons and slow pions that are reconstructed as tracks in the detector.

In the fit, both the bottom and charm asymmetries are to be determined. Therefore, the fit uses for each event its probabilities to be a correctly tagged $b\bar{b}$ or $c\bar{c}$ event or background, as determined from the simulation: The events are divided into several subsamples according to their $\mathcal{N}_b$, $\mathcal{N}_{bc}$, $\mathcal{N}_c$, and $|y|$ values. Three bins are used for each quantity, making a total of 81 subsamples separately for both electron and muon tagged events and 27 subsamples for the slow pion tagged events. These subsamples have different bottom and charm purities and are fitted simultaneously.

The cross-section for producing a $q\bar{q}$ pair is assumed to depend on y according to

$$\frac{d\sigma_{q\bar{q}}}{dy} \sim 1 + y^2 + \frac{8}{3} A_{FB}^{q} \, y \; . \tag{13}$$

The likelihood $\mathcal{L}_{sub}$ for one subsample is given by

$$\ln \mathcal{L}_{sub} = \sum_{candidates} \ln \left(1 + y^2 + \frac{8}{3} A_{FB}^{obs} \, y \right) \; , \tag{14}$$

where the sum is taken over all candidates in the subsample. The total likelihood is then given by the product of the likelihoods of all subsamples. The expected observed asymmetry A_{FB}^{obs} in each subsample is computed as

$$A_{FB}^{obs}(\mathcal{N}_b, \mathcal{N}_{bc}, \mathcal{N}_c, |y|) = \sum_{i=1}^{5} f_i(\mathcal{N}_b, \mathcal{N}_{bc}, \mathcal{N}_c, |y|) \, A_{FB}^{i} \; . \tag{15}$$

In this equation f_i denotes the predicted fraction of leptons or slow pions from source i, and A_{FB}^{i} is the corresponding asymmetry:

$$\begin{cases} A_{FB}^{1} = \quad (1 - 2\overline{\chi}_1^{eff}) \, A_{FB}^{b} & \text{for } b \to \ell \, , \\ A_{FB}^{2} = -(1 - 2\overline{\chi}_2^{eff}) \, A_{FB}^{b} & \text{for } b \to c \to \ell/\pi_s \, , \\ A_{FB}^{3} = \quad (1 - 2\overline{\chi}_3^{eff}) \, A_{FB}^{b} & \text{for } b \to \overline{c} \to \ell/\pi_s \, , \\ A_{FB}^{4} = \quad - A_{FB}^{c} & \text{for } c \to \ell/\pi_s \, , \text{ and} \\ A_{FB}^{5} = \quad 0 & \text{for background,} \end{cases} \tag{16}$$

where $\overline{\chi}_i^{eff}$ is the effective $B-\overline{B}$ mixing parameter. The fractions f_i have been calculated from the Monte Carlo simulation and depend on the mis-identification probability in each bin of $\mathcal{N}_b$,

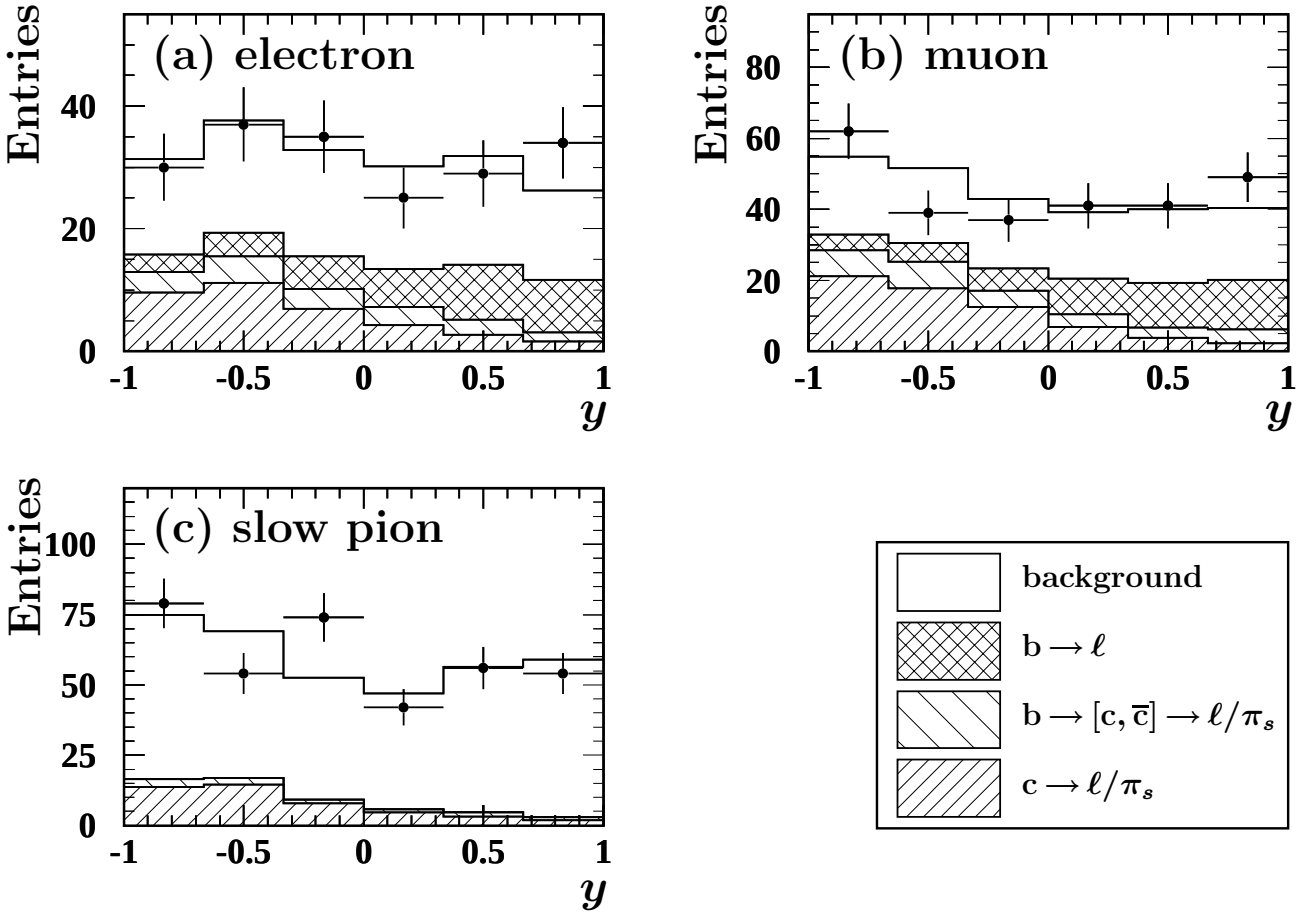

Figure 7: The y distributions of (a) electron, (b) muon, and (c) slow pion tagged events at a centre-of-mass energy of 189 GeV are given by the points with error bars. Also plotted is the expectation from the simulation together with the contributions from background (open histogram) and $\mathrm{b} \to \ell$ (cross-hatch), $\mathrm{b} \to [\mathrm{c}, \overline{\mathrm{c}}] \to \ell/\pi_s$ (wide diagonal hatch), and $\mathrm{c} \to \ell/\pi_s$ decays (narrow diagonal hatch). Note that in the fit, the tagged events are divided into subsamples of different bottom and charm purities to allow an extraction of both the bottom and charm asymmetries.

$\mathcal{N}_{\mathrm{bc}}$, $\mathcal{N}_{\mathrm{c}}$, and $|y|$, on the production rates of bottom and charm quarks, on the semileptonic branching ratios of heavy hadrons, and on the hadronisation fractions $f(\mathrm{b} \to [\mathrm{c}, \overline{\mathrm{c}}] \to \mathrm{D}^{*\pm})$ and $f(\mathrm{c} \to \mathrm{D}^{*+})$. Variations in the sample composition with $|\cos\theta_T|$ are taken into account since the f_i are binned in $|y|$. As described in Section 4.1, this likelihood fit has the advantage that the $|\cos\theta_T|$ dependence of the efficiency for identifying leptons and slow pions is not needed explicitly. The effective mixing parameters $\overline{\chi}_1^{\mathrm{eff}}$, $\overline{\chi}_2^{\mathrm{eff}}$, and $\overline{\chi}_3^{\mathrm{eff}}$ are determined from the simulation for each selected subsample of events. The mixing parameter $\overline{\chi} = 0.118 \pm 0.006$ [21] used in the simulation for inclusive $\mathrm{b\bar{b}}$ events is taken as an external input. The small non-zero contributions to the observed asymmetry from prompt leptons and slow pions from radiative and four-fermion events are accounted for, but left out of the above list for simplicity. The assumption that the backgrounds from mis-identified leptons and slow pions do not contribute to the observed asymmetry has been checked and will be discussed in Section 5.2.2.

The fit is done separately for the data taken at 133 GeV, 161 GeV, 172 GeV, 183 GeV, and 189 GeV. In Table 7, the numbers of lepton and slow pion tagged events are given, and the results of the fit for the bottom and charm asymmetries are summarised for each energy point together with the errors and correlations. The systematic errors have been evaluated as described in Section 5.2.

Energy	Electrons	Muons	Slow pions	Measured asymmetries	Correlation	Predicted asymmetries
133 GeV	48	69	82	$A_{\rm FB}^{\rm b} = -0.01\ ^{+0.37}_{-0.35} \pm 0.18$ $A_{\rm FB}^{\rm c} = 0.50\ ^{+0.31}_{-0.32} \pm 0.13$	+14%	$A_{\rm FB}^{\rm b,SM} = 0.48$ $A_{\rm FB}^{\rm c,SM} = 0.69$
161 GeV	16	37	42	$A_{\rm FB}^{\rm b} = 0.18\ ^{+0.56}_{-0.52} \pm 0.15$ $A_{\rm FB}^{\rm c} = 0.83\ ^{+0.59}_{-0.60} \pm 0.12$	+14%	$A_{\rm FB}^{\rm b,SM} = 0.55$ $A_{\rm FB}^{\rm c,SM} = 0.69$
172 GeV	14	29	20	$A_{\rm FB}^{\rm b} = 0.55\ ^{+0.85}_{-0.87} \pm 0.18$ $A_{\rm FB}^{\rm c} = 0.67\ ^{+0.49}_{-0.54} \pm 0.12$	+23%	$A_{\rm FB}^{\rm b,SM} = 0.56$ $A_{\rm FB}^{\rm c,SM} = 0.67$
183 GeV	77	104	126	$A_{\rm FB}^{\rm b} = 0.59\ ^{+0.29}_{-0.31} \pm 0.12$ $A_{\rm FB}^{\rm c} = 0.56\ ^{+0.27}_{-0.28} \pm 0.11$	+23%	$A_{\rm FB}^{\rm b,SM} = 0.57$ $A_{\rm FB}^{\rm c,SM} = 0.67$
189 GeV	190	269	359	$A_{\rm FB}^{\rm b} = 0.28 \pm 0.21 \pm 0.12$ $A_{\rm FB}^{\rm c} = 0.52\ ^{+0.18}_{-0.19} \pm 0.11$	+19%	$A_{\rm FB}^{\rm b,SM} = 0.58$ $A_{\rm FB}^{\rm c,SM} = 0.66$

Table 7: For each centre-of-mass energy, the numbers of lepton and slow pion tagged events, the results for the bottom and charm asymmetries as measured with the lepton and slow pion tag, and their correlation are listed. The first error is statistical, and the second systematic. In the last column, the Standard Model predictions for the asymmetries are given.

As a cross-check, the fit is also performed on the calibration data taken at the Z^0 peak in the years 1996, 1997, and 1998. The results of this fit are consistent with the average of LEP1 and SLD measurements given in [1].

4.5 Combination of the $A_{\rm FB}^{\rm b}$ Measurements

By construction, the samples used in the hemisphere charge analysis do not have any events in common with the lepton or slow pion tagged samples. The bottom asymmetry as measured with the vertex tag depends on the assumed value of the charm asymmetry, while the fit to the lepton and slow pion tagged events yields results for the bottom and charm asymmetries with a non-zero correlation. This dependence on the charm asymmetry has to be taken into account when combining the two bottom asymmetry measurements. The vertex tag measurement is applied as a constraint in the fit to the lepton and slow pion tagged events that is described in Section 4.4. Since the bottom and charm asymmetries are correlated in the fit to the lepton and slow pion tagged events, both the fitted bottom and charm asymmetries are expected to change in the constrained fit; but the error on the charm asymmetry is essentially unchanged.

The results for $A_{\rm FB}^{\rm b}$ and $A_{\rm FB}^{\rm c}$ are listed in Table 8 and are also shown in Figure 8 together with the Standard Model expectations as a function of the centre-of-mass energy. Good agreement is observed between the measurements and the predictions from ZFITTER.

Energy	Measured asymmetries	Correlation	Predicted asymmetries
133 GeV	$A_{\rm FB}^{\rm b} = 0.19 \pm 0.30 \pm 0.12$ $A_{\rm FB}^{\rm c} = 0.50\ ^{+0.31}_{-0.32} \pm 0.13$	+20%	$A_{\rm FB}^{\rm b,\,SM} = 0.48$ $A_{\rm FB}^{\rm c,\,SM} = 0.69$
161 GeV	$A_{\rm FB}^{\rm b} = -0.03\ ^{+0.45}_{-0.42} \pm 0.11$ $A_{\rm FB}^{\rm c} = 0.87\ ^{+0.58}_{-0.60} \pm 0.12$	+23%	$A_{\rm FB}^{\rm b,\,SM} = 0.55$ $A_{\rm FB}^{\rm c,\,SM} = 0.69$
172 GeV	$A_{\rm FB}^{\rm b} = 0.82\ ^{+0.67}_{-0.72} \pm 0.14$ $A_{\rm FB}^{\rm c} = 0.69\ ^{+0.49}_{-0.53} \pm 0.12$	+27%	$A_{\rm FB}^{\rm b,\,SM} = 0.56$ $A_{\rm FB}^{\rm c,\,SM} = 0.67$
183 GeV	$A_{\rm FB}^{\rm b} = 0.77\ ^{+0.23}_{-0.24} \pm 0.10$ $A_{\rm FB}^{\rm c} = 0.55\ ^{+0.27}_{-0.28} \pm 0.11$	+34%	$A_{\rm FB}^{\rm b,\,SM} = 0.57$ $A_{\rm FB}^{\rm c,\,SM} = 0.67$
189 GeV	$A_{\rm FB}^{\rm b} = 0.63\ ^{+0.15}_{-0.16} \pm 0.10$ $A_{\rm FB}^{\rm c} = 0.50\ ^{+0.18}_{-0.19} \pm 0.11$	+29%	$A_{\rm FB}^{\rm b,\,SM} = 0.58$ $A_{\rm FB}^{\rm c,\,SM} = 0.66$

Table 8: The results of the combined $A_{\rm FB}^{\rm b}$ and $A_{\rm FB}^{\rm c}$ measurements together with the Standard Model predictions from ZFITTER. The first error is statistical, and the second systematic.

In all asymmetry measurements, $R_{\rm c}$ and $R_{\rm b}$ are fixed to the Standard Model values as predicted by ZFITTER. The dependence of the measured values on the assumed values of $R_{\rm b}$ and $R_{\rm c}$ is parametrised as

$$\begin{aligned} \Delta A_{\rm FB}^{\rm b} &= a^{\rm b}(R_{\rm b})\ \frac{\Delta R_{\rm b}}{R_{\rm b}^{\rm SM}} + a^{\rm b}(R_{\rm c})\ \frac{\Delta R_{\rm c}}{R_{\rm c}^{\rm SM}} \\ \Delta A_{\rm FB}^{\rm c} &= a^{\rm c}(R_{\rm b})\ \frac{\Delta R_{\rm b}}{R_{\rm b}^{\rm SM}} + a^{\rm c}(R_{\rm c})\ \frac{\Delta R_{\rm c}}{R_{\rm c}^{\rm SM}}\ , \end{aligned} \tag{17}$$

where $\Delta R_{\rm q} = R_{\rm q} - R_{\rm q}^{\rm SM}$ for q=b, c. The Standard Model values for $R_{\rm b}$ and $R_{\rm c}$ are given in Table 9 together with the values of the coefficients $a^{\rm q}(R_{\rm q'})$.

Any systematic error from a common source (see Section 5 for the description of systematic uncertainties) is treated as fully correlated between the two measurements. However, there are large contributions to the systematic error that affect only one of the analyses, such that systematic errors are clearly no limitation to the combination of the two results.

5 Systematic Errors

In this section, the evaluation of the systematic errors for the analyses presented here is discussed. Both the secondary vertex and the lepton and slow pion tags depend crucially on the knowledge of the detector resolution for reconstructing charged particle tracks. Most of the other main systematic errors are independent for the two measurements.

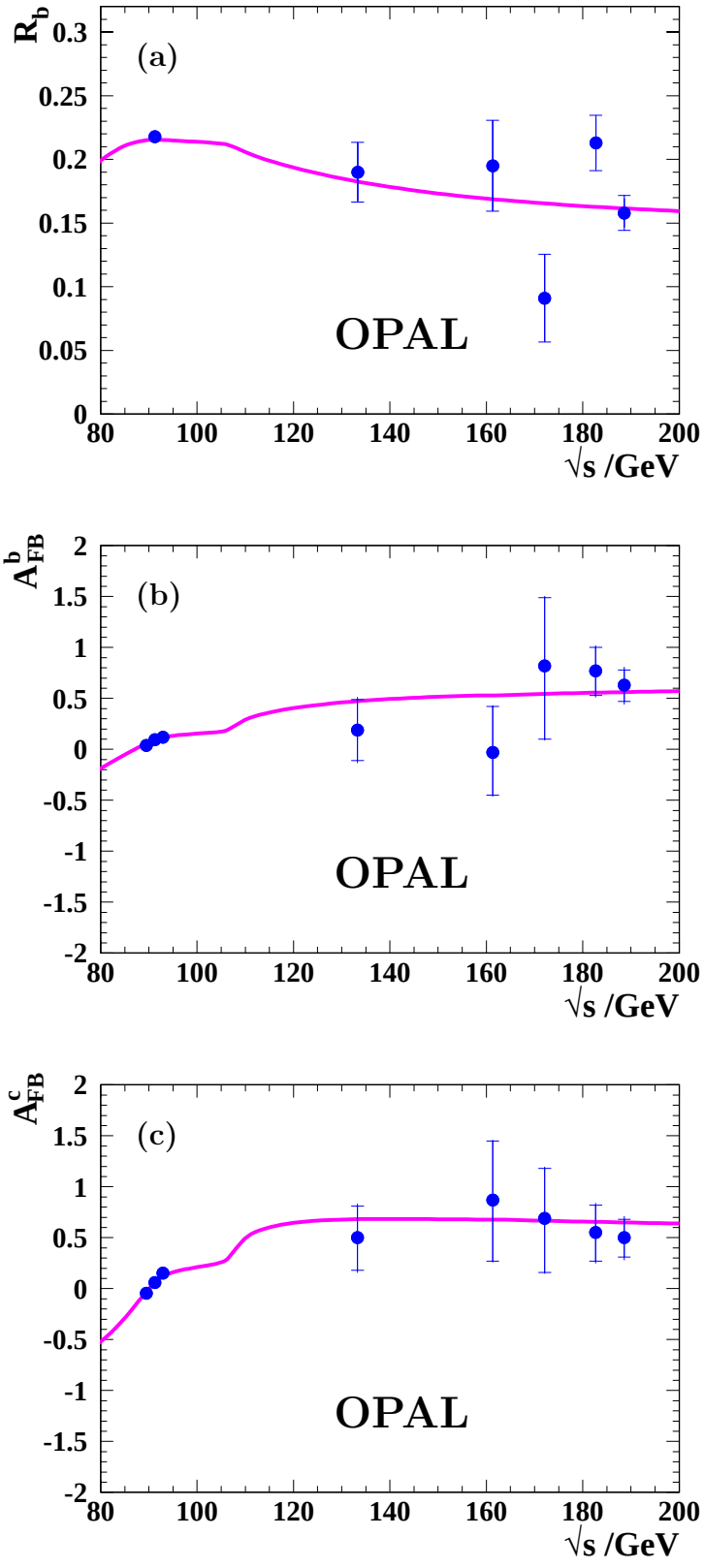

Figure 8: The R_{b}, $A^{\mathrm{b}}_{\mathrm{FB}}$, and $A^{\mathrm{c}}_{\mathrm{FB}}$ measurements are compared to the Standard Model predictions. The statistical and the total errors of the measurements are indicated. The measurements at $\sqrt{s} \approx m_{\mathrm{Z}^0}$ have been taken from [17,6,24,25]; here, the measurement errors are smaller than the points. The behaviour of the curve at $\sqrt{s} \approx 110$ GeV is due to the cut $\sqrt{s'/s} > 0.85$.

energy	R_b^{SM}	R_c^{SM}	$a^b(R_b)$	$a^b(R_c)$	$a^c(R_b)$	$a^c(R_c)$
133 GeV	0.184	0.223	−0.24	+0.12	+0.06	−0.28
161 GeV	0.171	0.244	−0.07	−0.06	+0.14	−0.86
172 GeV	0.168	0.249	−0.64	+2.48	+0.07	−0.11
183 GeV	0.165	0.253	−0.40	+0.21	+0.07	−0.36
189 GeV	0.164	0.255	−0.38	+0.23	+0.10	−0.30

Table 9: The Standard Model predictions for the partial hadronic decay widths R_b and R_c and the dependence of the results on their values are given. The coefficients apply to the combined measurements. The symbols are defined in the text.

5.1 Systematic Errors on R_b and A_{FB}^b with the Secondary Vertex Tag

In Table 10, a breakdown of the systematic error is given for both the R_b and A_{FB}^b measurements with the vertex tag at 189 GeV centre-of-mass energy. The systematic errors considered for these measurements are described in the following paragraphs.

Error source	ΔR_b	ΔA_{FB}^b
Event selection	0.0038	0.036
Final state QCD corrections	–	0.011
b fragmentation	0.0003	0.004
b decay multiplicity	0.0027	0.018
b hadron composition	0.0017	0.011
b lifetime	<0.0001	<0.001
c fragmentation	<0.0001	0.001
c decay multiplicity	<0.0001	0.003
c hadron composition	0.0011	0.011
c lifetime	<0.0001	<0.001
Four-fermion background	0.0009	<0.001
Monte Carlo statistics	0.0015	0.031
Track reconstruction	0.0051	0.057
Total systematic error	0.0074	0.078

Table 10: Systematic error breakdown for the R_b and the A_{FB}^b measurements with the vertex tag at $\sqrt{s} = 189$ GeV. Similar uncertainties have been determined for the other centre-of-mass energies.

5.1.1 Event Selection

The bias on the measurement of R_{b} from the selection of non-radiative events has already been discussed in Section 3.2. A correction has been applied, and an uncertainty of 100% is assigned to the correction. The uncertainty on the corrections for the interference between initial and final state radiation results in a systematic error of 0.5% on R_{b}. The contamination from radiative events has the effect of decreasing the measured asymmetry by 3%. The value is corrected accordingly, and a 3% systematic error is assigned. The likelihood fit is based on the assumption that the shape of the tagging efficiency as a function of $|\cos\theta_T|$ is the same for all flavours, which might not be true at the edges of the acceptance. The effect has been estimated by dividing the sample in bins of $|\cos\theta_T|$, over which the above assumption is valid, determing the asymmetry in each bin independently and comparing their average with the reference result. It has been found to affect the asymmetry by less than 1%, and is thus neglected.

5.1.2 Final State QCD Corrections

Final state QCD corrections are included in the calculation of the predictions with which the asymmetry measurements are compared. However, the experimental event selection is less efficient for events with hard gluon radiation due to the cuts on the decay length significance (for the vertex tag) and the lepton or slow pion momentum (for the lepton and slow pion analysis). The fraction of the QCD correction that has to be applied to the measurements has been determined previously at LEP1 and is typically between 0.3 and 0.6 [26]. The overall QCD corrections at $\sqrt{s} = 189\,\mathrm{GeV}$ have been determined from ZFITTER to be 0.015 for $A_{\mathrm{FB}}^{\mathrm{b}}$ and 0.022 for $A_{\mathrm{FB}}^{\mathrm{c}}$, respectively. Half of this correction is assigned as a systematic error.

5.1.3 Bottom and Charm Physics Modelling

Uncertainties in bottom and charm fragmentation and decay properties have been treated as follows:

- **b fragmentation:** Although the mean scaled energy $2\langle E_{\mathrm{b}}\rangle/\sqrt{s}$ of weakly decaying b hadrons is expected to change from LEP1 to LEP2 energies, the Peterson fragmentation parameter ϵ_P^{b}, which describes one step in the fragmentation process, is assumed not to vary with energy. Simulated $\mathrm{b\bar{b}}$ events are reweighted within the range of $0.0030 < \epsilon_P^{\mathrm{b}} < 0.0048$ [12], which corresponds to a variation of the mean scaled energy $2\langle E_{\mathrm{b}}\rangle/\sqrt{s}$ of weakly decaying b hadrons in Z^0 decays in the range of $2\langle E_{\mathrm{b}}\rangle/\sqrt{s} = 0.702 \pm 0.008$ [12].
- **b decay multiplicity:** The charged decay multiplicity of hadrons containing a b quark is varied in the Monte Carlo simulation according to [12].
- **b hadron composition:** The tagging efficiency differs for the various b hadron species. The fractions of b hadrons and their errors have been taken from [21]. The fractions $f(\mathrm{B}^0 + \mathrm{B}^+)$ and $f(\mathrm{B}_{\mathrm{s}}^0)$ are varied independently within their errors, and their variation is compensated by the b baryon fraction.
- **b hadron lifetimes:** The lifetimes of the different b hadrons are varied in the Monte Carlo by their errors according to [21].
- **c fragmentation:** $\mathrm{c\bar{c}}$ Monte Carlo events are reweighted by varying the Peterson fragmentation parameter ϵ_P^{c} in the range of $0.025 < \epsilon_P^{\mathrm{c}} < 0.031$ [12]. This corresponds to a

variation of the mean scaled energy $2\langle E_c\rangle/\sqrt{s}$ of weakly decaying c hadrons in Z^0 decays in the range of $2\langle E_c\rangle/\sqrt{s} = 0.484 \pm 0.008$.

- **c decay multiplicity:** The average charged track multiplicities of D^+, D^0 and D_s^+ decays are varied in the Monte Carlo within the ranges of the experimental measurements [27].
- **c hadron composition:** The D^0 fraction is written as $f(D^0) = 1 - f(D^+) - f(D_s^+) - f(c_{baryon})$. The last three parameters are varied independently by their errors according to [12] to evaluate the uncertainty on the charm efficiency.
- **c hadron lifetimes:** Charmed hadron lifetimes are varied within their experimental errors according to [21].

5.1.4 Four-fermion Background

Above the WW production threshold, the four-fermion background is largely dominated by W pairs. The uncertainty in the W pair production cross-section is taken into account and has been found to have a negligible systematic effect. The background from W pairs has the highest probability to be accepted in the tagged sample when one or both W bosons decay into a final state containing a charm quark. The systematic error on the W pair tagging efficiency is estimated by varying the charm physics modelling parameters as described above. The effect of the detector resolution is also taken into account, as described in Section 5.1.6.

5.1.5 Monte Carlo Statistics

Tagging efficiencies and charge identification probabilities are varied by the statistical error arising from the finite number of Monte Carlo simulated events.

5.1.6 Track Reconstruction

The effect of the detector resolution on the track parameters is estimated by degrading or improving the resolution of all tracks in the Monte Carlo simulation. This is done by applying a single multiplicative scale factor to the difference between the reconstructed and true track parameters. A $\pm 10\%$ variation is applied independently to the $r\phi$ and rz track parameters.

In addition, the matching efficiency for assigning measurement points in the silicon microvertex detector to the tracks is varied by 1% in $r\phi$ and 3% in rz. The systematic errors resulting from the individual variations are summed in quadrature.

5.2 Systematic Errors on A_{FB}^b and A_{FB}^c with the Lepton and Slow Pion Tag

Three different groups of systematic errors have been considered: those from detector effects, those related to physics models and external inputs used in the analysis, and effects introduced by the limited Monte Carlo statistics and the fitting procedure. A list of all systematic errors is given in Table 11.

Error source	$\Delta A_{\rm FB}^{\rm b}$	$\Delta A_{\rm FB}^{\rm c}$
Track reconstruction	0.088	0.070
Lepton and slow pion identification	0.009	0.013
Input modelling	0.045	0.022
Fragmentation modelling	0.024	0.033
Semileptonic decay models	0.007	0.005
Branching ratios	0.008	0.006
$\mathrm{B}-\overline{\mathrm{B}}$ mixing	0.003	0.001
Background asymmetries	0.024	0.066
Final state QCD corrections	0.008	0.011
Monte Carlo statistics	0.061	0.032
Fitting procedure	0.009	0.003
Total systematic error	0.122	0.111

Table 11: A breakdown of the systematic errors is given for the asymmetry measurement with leptons and slow pions at 189 GeV. Similar systematic errors have been obtained for the measurements at the other centre-of-mass energies above the Z^0 peak.

5.2.1 Detector Systematics

The lepton and slow pion identification relies on the proper modelling of the detector response in the Monte Carlo simulation.

- **Track Reconstruction:** The influence of the simulated detector resolution and matching efficiency for hits in the microvertex detector is estimated as described in Section 5.1.6.
- **Lepton Identification:** The fractions of misidentified electrons and muons are taken from Monte Carlo simulation. The modelling of the input variables to the artificial neural network for electron identification has been studied on Z^0 calibration data in a manner similar to that described in [17]. Differences between the data and the modelling in the Monte Carlo simulation have been determined using a pure sample of electrons from photon conversions and an inclusive sample of tracks depleted in conversion electrons. The dependence of the efficiency and background contamination of the selected electron sample on these differences has been studied, and the resulting uncertainties for each input have been added in quadrature. In addition, it has been shown that there is no large dependence of the resulting systematic error on the position of the $\mathcal{N}_{\rm el}$ cut. The systematic error has been evaluated separately for each year of data taking at energies above the Z^0 peak; the uncertainty on the efficiency is around 10%, and that on the background contamination around 20%.

  The performance of the muon tagging network has been studied on $\gamma\gamma \to \mu^+\mu^-$ events recorded at LEP energies above the Z^0 peak and on an inclusive sample of tracks from the Z^0 calibration data that fail the "best match" preselection criterion. The muon and background rates have been compared between data and Monte Carlo simulation in bins of $\mathcal{N}_\mu$, and the simulation has been reweighted to match the data distribution. The reweighting factors in each bin have been varied independently by their statistical errors, and the resulting variations of the measured asymmetries added in quadrature. For the inclusive muon sample selected with a cut at $\mathcal{N}_\mu > 0.65$, the reweighting factors for muon

signal and background are 0.95 ± 0.05 and 0.97 ± 0.04, respectively.

Conversion candidates are explicitly removed from the sample of events used in the fit. The $\mathcal{N}_{\rm cv}$ output distribution is well described in the simulation. The conversion finding efficiency is tested in the data using an algorithm which does not need the $\mathcal{N}_{\rm el}$ outputs for the two tracks as input. The accuracy of this test is 18%, and the conversion rate is varied by this amount to calculate the systematic error. The rate of non-prompt muons from pion and kaon decays in flight has been studied previously in [20], and has been found to be modelled to within 9%.

The four above systematic errors are added in quadrature to yield the value given in Table 11.

- **Slow Pion Efficiency:** Because of the large backgrounds in the slow pion sample, it is crucial to check that the slow pion reconstruction is modelled correctly in the Monte Carlo simulation. The efficiency has been studied by reconstructing slow pions in the Z^0 calibration data using the same cuts as described in Section 4.2.3, except for the upper momentum cut which has been lowered to $p_{\pi_s}^{\rm max}(\sqrt{s} = m_{Z^0}) = 4.17$ GeV. The slow pion content in this sample has been measured using a fit to the p_t^2 spectrum. Functions which are found to describe the shape of the background distribution well in the simulation are fitted to the p_t^2 sideband from 0.03 to 0.10 GeV^2. The number of signal slow pion events is then determined by extrapolating the background estimate to $p_t^2 = 0$ GeV^2. In the Z^0 calibration data, this fit has a relative statistical precision of 6%, but an additional systematic error of 23% is assigned to cover biases resulting from the extrapolation procedure and the particular choice of fit function.

  Combining this result with the OPAL measured yield of D^{*+} mesons in hadronic Z^0 decays of $\bar{n}_{Z^0 \to D^{*+}X} = 0.1854 \pm 0.0041 \pm 0.0059 \pm 0.0069$ [22], the efficiency of the slow pion reconstruction in Z^0 decays is measured to be $(37.3 \pm 9.0)\%$, where the relative errors of 6% and 23% have been added in quadrature. This is consistent with the value in the simulation of $(31.9 \pm 1.5(\text{stat.}))\%$. The fractional error on the slow pion efficiency is then assigned to the slow pion efficiencies at energies above the Z^0 peak, which are taken from the simulation. In order to determine the systematic error on the asymmetry measurements, the expected number of slow pions in each of the different subsamples is varied according to the error on the efficiency, and balanced by the expected number of background events so that the total number of tagged events is kept constant.

  No additional systematic error is assigned for the modelling of the shape of the slow pion signal p_t^2 distribution since the signal shape in Z^0 decays has been found to be well described in the simulation.

- **Modelling of Artificial Neural Network Inputs:** Each of the input distributions used in the flavour separation networks has been compared between data and Monte Carlo simulation. The simulated distributions are reweighted for each input variable in turn to agree with the corresponding data distributions, and the analysis is repeated with the weighted events. The observed differences from the original fit result are added in quadrature to yield the systematic uncertainty due to the modelling of the input variables.

5.2.2 Physics Systematics

The fragmentation of charm and bottom quarks and the momentum spectra of leptons emitted in their semileptonic decay are described using phenomenological models tuned to experimental data. Systematic errors introduced by models of heavy hadron semileptonic decays, by the use of externally measured inputs, and from the assumed asymmetries of background candidates are assessed as follows:

- **Lifetimes:** The lifetimes of weakly decaying b- and c-flavoured hadrons are varied as described in Section 5.1.3. The resulting changes in measured asymmetries are negligible.
- **Fragmentation:** Bottom and charm fragmentation uncertainties are estimated as described in Section 5.1.3.
- **Semileptonic Decay Models:** Systematic effects due to the modelling of semileptonic decays of heavy hadrons are studied following the recommendations in [12]. The lepton momentum spectra in the Monte Carlo simulation are reweighted to different theoretical models, with ranges of parameters chosen such that the experimental errors are covered.
- **Branching Ratios and Hadronisation Fractions:** The values for the semileptonic branching ratios $B(\mathrm{b} \to \ell)$, $B(\mathrm{b} \to \mathrm{c} \to \ell)$, $B(\mathrm{b} \to \overline{\mathrm{c}} \to \ell)$, and $B(\mathrm{c} \to \ell)$ are taken from [12], and they are varied within their errors. Similarly, the values for the hadronisation fractions $f(\mathrm{b} \to \mathrm{c} \to \mathrm{D}^{*+})$ and $f(\mathrm{c} \to \mathrm{D}^{*+})$ are taken from [22] and varied within their errors.

  In the absence of any measurements, the hadronisation fraction $f(\mathrm{b} \to \overline{\mathrm{c}} \to \mathrm{D}^{*-})$ is taken from the simulation and varied by 100% in order to assess the systematic error.
- **$\mathrm{B}-\overline{\mathrm{B}}$ Mixing:** The $\mathrm{B}-\overline{\mathrm{B}}$ mixing parameter is taken as an external input. The value of $\overline{\chi} = 0.118 \pm 0.006$ [21] is used, and the variation within its error yields the systematic uncertainty listed in Table 11.
- **Background Asymmetries:** Prompt leptons and slow pions from four-fermion background in the selected event sample can affect the measured asymmetries. They may lead to a rather large observed forward-backward asymmetry, but their contribution to the overall sample is small. The asymmetry from these events is varied within ± 0.5 to determine the systematic error. The error due to the uncertainties on the bottom and charm asymmetries in radiative events is negligible.

  The asymmetry in the y distribution of mis-identified lepton and slow pion candidates is assumed to be zero for any event type. For lepton candidates, this assumption is verified within an accuracy of 2% on an inclusive sample of tracks that pass the lepton momentum cuts and do not pass the cut on $\mathcal{P}_{\mathrm{sig}}$. For slow pions, a sample of tracks that pass the cuts on the slow pion momentum and transverse momentum, but do not pass the cut on $\mathcal{P}_{\mathrm{sig}}$, is used. The asymmetry of slow pion background is found to be zero with an error of 4%. The asymmetries from lepton and slow pion backgrounds are then varied within these limits to assess the associated systematic errors.

  All the above errors are added in quadrature to yield the uncertainty given in Table 11.
- **Final State QCD Corrections:** As described in Section 5.1.2, half the QCD correction to $A_{\mathrm{FB}}^{\mathrm{b}}$ and $A_{\mathrm{FB}}^{\mathrm{c}}$ as computed using ZFITTER is assigned as systematic error.

5.2.3 Monte Carlo Statistics

An error arises from the limited statistics in the Monte Carlo simulation that is used to predict the fractions f_i for each subsample (see Section 4.4). This uncertainty has been evaluated by varying for each subsample in turn the contribution from each source by its statistical error, redoing the fit, and adding all observed differences in quadrature.

5.2.4 Fitting Procedure

The fitting procedure has been studied in a large number of simulated experiments with the same statistics as in the actual measurements. It has been found to be essentially unbiased for the large data samples recorded at 183 GeV and 189 GeV. For the datasets at 133 GeV, 161 GeV, and 172 GeV, however, the statistical error from the fit has been found to be underestimated by a factor of up to 1.16 (bottom) or 1.05 (charm asymmetry), and biases of up to $0.12\,\sigma$ and $0.06\,\sigma$ have been found for the fitted bottom and charm asymmetry, respectively, where in each case σ denotes the statistical error. The statistical errors are adjusted, the measurements are corrected according to the observed biases, and the full bias is treated as an additional systematic error.

5.2.5 Cross-Checks

Consistent results are observed when the fit is repeated with the numbers of bins in $\mathcal{N}_{\mathrm{b}}$, $\mathcal{N}_{\mathrm{bc}}$, $\mathcal{N}_{\mathrm{c}}$, and $|y|$ varied independently between 2 and 4. In addition, all selection cuts have been varied, with no significant deviations in the results. Consistent results have been found when the slow pion tagged events are not used in the fit. In the 189 GeV data sample, the statistical error of the charm asymmetry increases from 0.18 to 0.21 without the information from slow pion tagged events, while the error on the bottom asymmetry stays the same.

6 Conclusions

Using data collected at centre-of-mass energies between 130 GeV and 189 GeV with the OPAL detector at LEP, the relative $\mathrm{e^+e^-} \to \mathrm{b\overline{b}}$ production rate and the forward-backward asymmetries in $\mathrm{e^+e^-} \to \mathrm{b\overline{b}}$ and $\mathrm{e^+e^-} \to \mathrm{c\overline{c}}$ production have been measured to be

Energy	R_{b}	$A_{\mathrm{FB}}^{\mathrm{b}}$	$A_{\mathrm{FB}}^{\mathrm{c}}$
133 GeV	$0.190 \pm 0.023 \pm 0.007$	$0.19 \pm 0.30 \pm 0.12$	$0.50\ ^{+0.31}_{-0.32} \pm 0.13$
161 GeV	$0.195 \pm 0.035 \pm 0.007$	$-0.03\ ^{+0.45}_{-0.42} \pm 0.11$	$0.87\ ^{+0.58}_{-0.60} \pm 0.12$
172 GeV	$0.091 \pm 0.034 \pm 0.005$	$0.82\ ^{+0.67}_{-0.72} \pm 0.14$	$0.69\ ^{+0.49}_{-0.53} \pm 0.12$
183 GeV	$0.213 \pm 0.020 \pm 0.009$	$0.77\ ^{+0.23}_{-0.24} \pm 0.10$	$0.55\ ^{+0.27}_{-0.28} \pm 0.11$
189 GeV	$0.158 \pm 0.012 \pm 0.007$	$0.63\ ^{+0.15}_{-0.16} \pm 0.10$	$0.50\ ^{+0.18}_{-0.19} \pm 0.11$

where in each case, the first error is statistical and the second systematic. These values are illustrated in Figure 8 together with the dependences on the centre-of-mass energy as predicted

in the Standard Model. For all measurements, good agreement is observed with the Standard Model expectation. The measurements of $b\bar{b}$ production presented in this paper supersede the previously published values of references [4, 5].

References

[1] For a recent overview, see:
The 4 LEP experiments: ALEPH, DELPHI, L3 and OPAL, the LEP Electroweak Working Group, and the SLD Heavy Flavour and Electroweak Groups, *A Combination of Preliminary Electroweak Measurements and Constraints on the Standard Model,* CERN-EP/99-015, 8th February 1999.

[2] ALEPH Collaboration, R. Barate et al., *Study of Fermion Pair Production in* e^+e^- *Collisions at 130–183 GeV,* CERN-EP/99-042, 3rd March 1999, submitted to Eur. Phys. J. **C**.

[3] DELPHI Collaboration, P. Abreu et al., *Measurement and Interpretation of Fermion-Pair Production at LEP energies from 130 to 172 GeV,* CERN-EP/99-005, (January 1999), submitted to Eur. Phys. J. **C**.

[4] OPAL Collaboration, K. Ackerstaff et al., Eur. Phys. J. **C2** (1998) 441.

[5] OPAL Collaboration, K. Ackerstaff et al., Eur. Phys. J. **C6** (1999) 1.

[6] OPAL Collaboration, G. Alexander et al., Z. Phys. **C70** (1996) 357.

[7] OPAL Collaboration, K. Ahmet et al., Nucl. Instrum. Methods **A305** (1991) 275;
O. Biebel et al., Nucl. Instrum. Methods **A323** (1992) 169;
M. Hauschild et al., Nucl. Instrum. Methods **A314** (1992) 74;
B.E. Anderson et al., IEEE Transactions on Nuclear Science **41** (1994) 845;
S. Anderson et al., Nucl. Instrum. Methods **A403** (1998) 326.

[8] JADE Collaboration, W. Bartel et al., Z. Phys. **C33** (1986) 23;
JADE Collaboration, S. Bethke et al., Phys. Lett. **B213** (1988) 235.

[9] OPAL Collaboration, M.Z. Akrawy et al., Z. Phys. **C49** (1991) 341.

[10] PYTHIA 5.721 and JETSET 7.408 generators: T. Sjöstrand, Comp Phys Comm. **82**, (1994), 74; T. Sjöstrand, LUTP 95-20.

[11] C. Peterson, D. Schlatter, I. Schmitt, and P. M. Zerwas, Phys. Rev. **D27** (1983) 105.

[12] The LEP Collaborations, ALEPH, DELPHI, L3 and OPAL, Nucl. Instrum. Methods **A378** (1996) 101.

Updated averages are described in "Input Parameters for the LEP Electroweak Heavy Flavour Results for Summer 1998 Conferences", LEPHF 98-01 (see http://www.cern.ch/LEPEWWG/heavy/).

[13] J. Fujimoto et al., Comput. Phys. Commun. **100** (1997) 128.

[14] J. Allison et al., Nucl. Instrum. Methods **A317** (1992) 47.

[15] OPAL Collaboration, R. Akers et al., Z. Phys. **C66** (1995) 19.

[16] OPAL Collaboration, K. Ackerstaff et al., Z. Phys. **C74** (1997) 1.

[17] OPAL Collaboration, G. Abbiendi et al., Eur. Phys. J. **C8** (1999) 217.

[18] D. Bardin et al., CERN-TH 6443/92 (May 1992); Phys. Lett. **B255** (1991) 290; Nucl. Phys. **B351** (1991) 1; Z. Phys. **C44** (1989) 493;
we use ZFITTER version 6.21 with default parameters, except `FINR`=0 and `INTF`=0, and with the following input parameters: $m_{\rm Z}$=91.1863 GeV, $m_{\rm top}$=175 GeV, $m_{\rm Higgs}$=130 GeV, $\alpha_{\rm em}(m_{\rm Z})$=1/128.896, $\alpha_{\rm s}(m_{\rm Z})$=0.118.

[19] M. Consoli, W. Hollik, and F. Jegerlehner, *Electroweak radiative corrections for* $\rm Z^0$ *physics,* in *Proceedings of the Workshop on* $\rm Z^0$ *Physics at LEP1,* CERN 89-08, Vol. 1, 7.

[20] OPAL Collaboration, R. Akers et al., Z. Phys. **C65** (1995) 17.

[21] Particle Data Group, C. Caso et al., Eur. Phys. J. **C3** (1998) 1.

[22] OPAL Collaboration, K. Ackerstaff et al., Eur. Phys. J. **C1** (1998) 439.

[23] OPAL Collaboration, R. Akers et al., Z. Phys. **C66** (1995) 555.

[24] OPAL Collaboration, K. Ackerstaff et al., Z. Phys. **C75** (1997) 385.

[25] OPAL Collaboration, G. Alexander et al., Z. Phys. **C73** (1997) 379.

[26] LEP Heavy Flavor Working Group, D. Abbaneo et al., Eur. Phys. J. **C4** (1998) 185.

[27] MARK III Collaboration, D. Coffman et al., Phys. Lett. **B263** (1991) 135.